DISTURBANCE WAVE DEVELOPMENT IN TWO-PHASE GAS-LIQUID UPWARDS VERTICAL ANNULAR FLOW

Yujie Zhao[a], Christos N. Markides[b,*], Omar K. Matar[c] and Geoffrey F. Hewitt[d]

Imperial College London, South Kensington Campus, London SW7 2AZ

[a] yujie.zhao@imperial.ac.uk
[b] c.markides@imperial.ac.uk
[c] o.matar@imperial.ac.uk
[d] g.hewitt@imperial.ac.uk

ABSTRACT

Disturbance waves are of central importance in annular flows. Such waves are characterised by their large amplitudes relative to the mean film thickness, their high translation velocities relative to the mean film speed, and their circumferential coherence. The present paper is concerned with the existence, development and translation of disturbance waves in upwards, gas-liquid annular flows. Experiments are described, which featured simultaneous high-frequency film thickness measurements from multiple conductance probes positioned circumferentially and axially along a vertical pipe, that were aimed at studying the three-dimensional development of these interfacial structures as a function of distance from the tube inlet. From the results, it is found that disturbance waves begin to appear and to achieve their circumferential coherence from lengths as short as 5 – 10 pipe diameters downstream of the liquid injection location; this coherence gradually strengthens with increasing distance from the inlet. It is further shown that the spectral content of the entire interfacial wave activity shifts to lower frequencies with increasing axial distance from the inlet, with the peak frequency levelling off after approximately 20 pipe diameters. Interestingly, on the other hand, the frequency of occurrence of the disturbance waves first increases away from the inlet as these waves form, reaches a maximum at a length between 7.5 and 15 pipe diameters that depends on the flow conditions, and then decreases again. This trend becomes increasingly evident at higher gas and/or liquid flow-rates. Both wave frequency measures increase monotonically at higher gas and/or liquid flow-rates.

***Keywords**:* gas-liquid flow; vertical annular flow; film thickness; wave frequency; coherence; disturbance waves

[*] Corresponding author. Tel.: +44 20 759 41601. E-mail: c.markides@imperial.ac.uk

1. INTRODUCTION

Annular flow is a regime of two-phase, gas-liquid flow that occurs in a wide range of practical applications, including transfer lines (e.g. gas-liquid oil wells), evaporators and condensers (Hewitt and Hall-Taylor 1970; Andreussi *et al.* 1985; Schadel *et al*. 1990; Alekseenko *et al*. 1994, 2009; Pan and Hanratty 2002; Park *et al.* 2004). This flow regime corresponds to a situation in which the liquid phase flows in the form of a film on the inside of the conduit wall, in addition to droplets entrained within the gas phase. Understanding the intricate interfacial dynamics of annular flows is important for a number of reasons, which include the ability to predict the frictional pressure drop in two-phase flows (Wallis 1969; Asali *et al.* 1985; Fukano and Furukawa 1998; Fore *et al.* 2000; Wongwises and Kongkiatwanitch 2001; Wang and Gabriel 2005; Belt *et al.* 2009) that dictate pumping requirements, the fraction of liquid entrained in the gas in the form of droplets (Andreussi 1983; Schadel *et al.* 1990; Ambrosini *et al.* 1991; Azzopardi 1997; Pan and Hanratty 2002; Sawant *et al.* 2008a) and the onset of flooding in counter-current configurations (Dukler *et al.* 1984; McQuillan and Whalley 1985; Govan *et al.* 1991; Karimi and Kawaji 2000). Although both upwards and downwards annular flows have been studied in the literature, in this paper we focus on the vertical, upwards (co-current) gas-liquid flow configuration.

An important feature of annular flows is the formation of waves at the film/core interface. One of the most characteristic and important interfacial wave phenomena in annular flow is the formation of large waves (known as *disturbance waves*) at the interface (Taylor 1963; Hewitt 1969; Hewitt and Hall-Taylor 1970; Azzopardi 1986, 1997; Alekseenko *et al*. 1994, 2009). Disturbance waves have been observed above a threshold liquid flow-rate value, and remain correlated over considerable distances. Achieving a fundamental understanding of the mechanisms underlying the onset and evolution of disturbance waves is important for a number of reasons. For instance, it seems likely that (at least at low liquid viscosities) disturbance waves are a necessary condition for the entrainment of droplets from wavy interfaces (Cousins *et al*. 1965; Cousins and Hewitt 1968a, 1968b; Hewitt and Roberts 1969; Azzopardi 1986, 1997; Owen and Hewitt 1986, Pan and Haratty 2002; Sawant *et al.* 2008a; Alekseenko *et al.* 2009). Disturbance waves also have a dominant role in the shear stress at the interface in annular flow and measurements of wall-shear stress underneath such waves are reported by Martin (1983) who made simultaneous measurements at the same locality of shear stress (using a hot film probe device) and film thickness (using a conductance probe device). The large film thickness associated with the disturbance waves also corresponded to a large wall shear stress. In recent work, Wongwises and Kongkiatwanitch (2001) used a combination of flush-mounted wall electrodes to measure the film thickness, and an isokinetic probe connected to a cyclone separator to measure the effect of interfacial structure on the gas-liquid interfacial friction factor. The effect of liquid viscosity on the film structure, entrained fraction, and friction factor in upwards annular flow was investigated (McNeil and Stuart 2003). Wang and Gabriel (2005) also used conductance probes to obtain information about the film structure and its effect on the interfacial roughness and friction factor.

Unsurprisingly, disturbance waves also have a profound influence on heat transfer in annular flow. Traditional methods of predicting heat transfer in these systems based on turbulent boundary layer theory, and assuming average values for the film thickness and interfacial shear stress (see Hewitt and Hall-Taylor 1970), grossly over-predict the heat transfer rate, which is to be expected due to the essentially intermittent nature of the flow. The

computational fluid dynamics (CFD) study of Jayanti and Hewitt (1997) included predictions of heat transfer in annular flow with disturbance waves. The disturbance wave regions were predicted to be zones of high heat transfer rate, whereas the laminar substrate regions between the waves were comparatively low heat transfer ones. On average, the heat transfer rate was found to be lower than that predicted from the corresponding average shear stress and film thickness, in reasonable agreement with experimental observations. The high heat transfer coefficient between the waves should imply larger suppression of nucleate boiling. However, high-speed visual observations of boiling in these flows have indicated that nucleate boiling occurs preferentially in the disturbance waves regions (Barbosa *et al*. 2002). This apparently contradictory behaviour might possibly be explained by a *fall* of pressure (and hence a *fall* in saturation temperature) in a disturbance wave region. The mechanism for such a reduction in pressure is discussed by Hewitt *et al*. (1996). The flow of the vapour over the substrate region would be typical of a turbulent flow over a relatively flat surface. In the disturbance wave region, the surface is highly roughened and the velocity profile becomes more parabolic in shape. The change from the flat parabolic profile requires a reduction in pressure (as the momentum flux of the gases increase) and this might explain the apparent anomaly.

The study of disturbance waves has been an on-going topic in two-phase flow and amongst recent publications one may cite the work of Sekoguchi *et al.* (1985), Sekoguchi and Takeishi (1989), Wang *et al.* (2004), Schubring *et al.* (2010a, 2010b, 2010c) and Okawa *et al.* (2010). A review on the topic of disturbance waves in annular flow is given by Azzopardi (1986). The works by Sekoguchi and his co-investigators concentrated on characterising the disturbance wave region; of particular note was the observation of a special type of wave (the *huge wave*) in annular flow under certain circumstances. Wang *et al.* (2004) concentrate on the influence of wave height on interfacial friction and Sawant *et al.* (2008b) refer to new correlations that they have developed for disturbance wave frequency. In the work by Schubring and his collaborators detailed visualisation techniques are applied to the study of disturbance waves, while liquid film behaviour under oscillation conditions has been studied by Okawa *et al.* (2010). A missing piece of information about disturbance waves has been the nature of their formation at the channel entrance, and particularly with the development of circumferential ring-like structures in the waves. This is the main focus of the present work.

A number of investigations have been devoted to the measurement of the detailed characteristics of disturbance waves. High-speed imaging studies (Hewitt and Lovegrove 1969) have shown that the disturbance wave regions are disturbed zones, having a 'milky' appearance, which extend for about one tube diameter in length. The same studies have also shown that the disturbance waves are advected along the tube for long distances (although they occasionally coalesce). The peak amplitude of the disturbance waves was determined by Hewitt and Nicholls (1969) using a fluorescence technique since the conductance probes used in early work saturate at higher film thickness and do not give reliable information of peak amplitude. It was found that the amplitudes of disturbance waves were typically 5 – 6 times the mean film thickness. Hall-Taylor and Nedderman (1969) used a conductance probe device to measure the frequency of waves on the tube surface as a function of distance from the liquid injector (in this case, the liquid was injected smoothly using a porous wall section). The results obtained by Hall-Taylor and Nedderman (1969) are illustrated in Figure 1 and it will be seen that the frequency decreases with distance tending towards an asymptotic value at long distance. These authors also suggested that the decrease in frequency is due to coalescence of the waves resulting from a dispersion of their velocity.

More recently, Han *et al.* (2006) used a parallel wire probe to obtain disturbance wave shapes and velocities across a wide range of gas and liquid flow-rates. Alekseenko *et al.* (2009) employed high-speed planar laser-induced fluorescence (PLIF) to observe the development of two types of waves in downward annular flows under entrainment and no-entrainment conditions. The authors termed the first type 'disturbances' and 'primary' waves under entrainment and no-entrainment conditions, respectively, while the second type of waves was referred to as 'secondary'. The latter waves were always found to occur on the back-slopes of the former and catch up with them under entrainment conditions; this no longer occurs in no-entrainment conditions. Schubring *et al*. (2010b, 2010c) also used PLIF to visualise the liquid film in vertical, upwards annular flow, and to show that its average thickness increases with liquid flow-rate and decreases with gas flow-rate, while Kaji and Azzopardi (2010) examined the formation of disturbance waves in upward annular flow and showed that their speeds can be predicted successfully using existing correlations at low liquid flow-rates only.

In addition to the experimental work, a number of numerical studies were also performed. Jayanti and Hewitt (1997) calculated the characteristics of disturbance waves in annular flow using CFD. The authors concluded that the waves were regions of high turbulence separated by an essentially laminar substrate film. The link between disturbance waves and turbulence had been suggested by Martin and Azzopardi (1985). Han *et al.* (2006) used a steady re-normalisation group (RNG) k–ε model the turbulent gas flow in vertically upwards annular flow configurations coupled to a physical model for the film that accounted for droplet entrainment, variable wave velocity and gravitational forces.

Although the subject of interfacial disturbance waves in upwards and downwards annular flow has received considerable attention in the literature, there remains an open question regarding the development of the coherence of these waves in the circumferential direction. This is an important issue related to the mechanism underlying the transition from complex, three-dimensional interfacial structures to essentially two-dimensional, circumferentially coherent waves, which has not been addressed adequately. For instance, the results obtained by Hall-Taylor and Nedderman (1969) were obtained for one position around the tube periphery and there is no evidence from that work about the development of a coherent circumferential structure. The more recent PLIF results of Schubring *et al*. (2010b, 2010c) were also concerned with a single circumferential position.

That such circumferential coherence exists is partly evidenced by the work Hewitt and Lovegrove (1969) who showed that the disturbance waves are coherent around the periphery of the tube approximately 2.6 m downstream of the liquid injector. This was done by having four conductance probes spaced at 90° intervals around the tube and recording their simultaneous output. To the best of the authors' knowledge, there is no evidence about the process of formation of these coherent structures in the region immediately upstream of the liquid injection location. The objective of the present work is to investigate this region in detail and to provide new insights into the mechanisms of disturbance wave formation and their three-dimensional spatio-temporal development.

The rest of this paper is organised as follows; in Section 2, we provide a brief description of the experimental setup, data-acquisition techniques and calibration methods. In Section 3, we present our results, which include time-traces of the film thickness at various axial and circumferential locations for varying gas and liquid flow-rates, and a statistical analysis of

these data that demonstrate the emergence of circumferentially coherent disturbance waves; the axial length over which coherence is achieved is measured and plotted as a function of system parameters. Finally, concluding remarks are provided in Section 4.

2. EXPERIMENTAL METHODOLOGY

The principal objective of the experiments described herein was to make measurements of the thickness of the liquid film in annular flow as a function of gas and liquid flow-rates and circumferential and axial position, in order to elucidate the evolution of the disturbance waves to their terminal state along the channel. In addition to the characteristics of the liquid film, measurements were also made of the pressure gradient and these are also reported.

A schematic diagram of the experimental apparatus is shown in Figure 2. The gas (site mains air at 7 bar) is fed to the bottom of a vertical tube with inner diameter $D = 34.5$ mm. The liquid (a closed loop of water with added potassium nitrate salt to enhance its electrical conductivity for the electrical capacitance measurements) is circulated by a pump around the loop and introduced around the periphery of the tube at a distance of 0.733 m (or, 0.21 D) from the air inlet to allow the air flow to develop. The water flow-rate was measured by pre-calibrated rotameter with an accuracy of ±5%, and the air flow-rate was set and measured by a digital mass flow controller (MFC) with an accuracy of ±1%.

Commonly, in experiments on annular film the liquid film is introduced through a porous wall section. In the present experiments it was preferred to use a conical injector system as shown in Figure 3. It was considered that such an injector would give a more reliably uniform flow around the periphery and would also allow the film to be introduced at a specific location. Conical injection systems of this type are used for this reason in industrial practice in, for instance, the manufacture of detergents.

The main quantity being measured in the experiments was that of liquid film thickness, δ, for which a variety of techniques are available, e.g. see Hewitt (1982). Perhaps the most widely employed technique has been the use of conductance measurements between electrodes manufactured to be flush with the inside surface of the tube (Wang and Gabriel 2005). Though convenient and inexpensive, this type of method has certain disadvantages, which include the fact that the film thickness measurement is an *average* over the spatial region of influence of a probe, and that conductance probes of this kind have a natural limitation; for large film thicknesses the response becomes more insensitive to the film thickness. The conductance measured between the electrodes of the probes increases linearly with film thickness, but asymptotes to a constant value as the film thickness gets larger; the smaller the probe, the smaller the linear region. Thus, selecting these probes for this kind of measurement is a matter of optimising the localisation of the measurement and the ability to measure thick films. Thus, there is a balance to be struck between the localisation (or, the spatial resolution) of the measurement (which implies probes which are closely spaced) and the need for an adequate response at high film thicknesses (which implies larger spacing of the probes). In addition, the close proximity of the probes in our work also demands attention; the use of earthed outer rings assisted in minimising the interference between the probes placed around the periphery of the tube. Alternative techniques such as fluorescence are more effective in obtaining localised measurements (see for instance the original work of Hewitt and Nicholls (1969), Alekseenko *et al.* (2009), Schubring *et al.* (2010b, 2010c), and the recent efforts by

Morgan *et al*. (2012a, 2012b) in a horizontal two-phase (liquid-liquid) flow, Farias *et al.* (2012) in a horizontal annular two-phase (gas-liquid) flow, and Zadrazil *et al*. (2012) in a *downwards* gas-liquid annular flow), but the deployment of multiple fluorescence systems, or a multi-planar fluorescence system for the simultaneous measurement of planes around the pipe periphery, is much more difficult and expensive than that of film conductance devices.

In an early demonstration of the circumferential coherence of disturbance waves, Hewitt and Lovegrove (1969) employed "two-pin" probes spaced equally around the tube diameter at a fixed distance from the inlet. Although these measurements suggested the existence of circumferential coherence, there are problems in using this kind of probe when the distance between the probes is limited; this is because the probes can tend to interfere with one another leading to a false positive indication. In the present experiments, "concentric" probes were employed instead, as illustrated in Figure 4. Note that, two such sections (each featuring a set of four probes) were used in our experiments, one with the probes numbered 1-4 shown in Figure 4, and a second identical section (not shown here) with probes numbered 5-8. The probe sections and the embedded sets of probes could be moved within the test section to look at correlations between probes not only in the circumferential direction but also in the axial direction. In the probes used, the central pin was 3.2 mm in diameter and the outer ring had an internal diameter of 13.2 mm and an outer diameter of 13.4 mm. The surface of the probe was machined during manufacture so that it was flush with the inside surface of the 34.5 mm tube. A special flanged section held the conductance probes and four such probes were placed around the periphery at an equal 90° circumferential spacing. The advantage of the revised "concentric" design shown in Figure 4 is that all outer rings can be maintained at earth potential. This minimises the interference between the four probes around the pipe circumference and allows local measurements to be made.

The conductance of the liquid film across the probes was measured using a custom designed and built electrical circuit. An alternating current (AC) source at 5 kHz feeds current through a fixed resistor and then through the probe to earth. The current drawn from the circuit creates a voltage drop across the fixed resistor and the conductance between the probe electrodes can be related to this voltage drop. The relationship is not precisely linear, and specifically there is a drop in the sensitivity of the potential divider (a voltage drop) as the impedance in the power supply box changes. The voltage measured by the system was low-pass filtered at 500 Hz in order to circumvent aliasing in the output signal, and then fed to a PCI-DAS1200 acquisition card on a computer. The acquisition frequency was 1000 Hz.

In order to convert the conductance probe voltage registered by the data acquisition system to film thickness, the following steps were made:

(1) By replacing the conductance probe with a series of fixed resistors, the relationship between conductance (G) and voltage (V) could be established. This relationship was fitted using a 3rd order polynomial as is illustrated in Figure 5.

(2) The measured conductance was converted into a non-dimensional conductance G^* via the relationship,

$$G^* = \frac{G}{c\left(d_2 - d_1\right)}, \qquad (1)$$

where c is the specific conductivity (Siemens/m) of the liquid phase, d_1 the diameter of the inner electrode (0.0032 m) and d_2 the diameter of the inner surface of the outer ring (0.0132 m). To enhance the conductance of the liquid (aqueous) phase, potassium nitrate was added to the circulating water with a concentration of 0.594 kg/m^3. The specific conductivity of the liquid was measured using a JENWAY PTI-18 digital conductivity meter and found to be 8.32×10^{-2} Siemens/m.

(3) Probes of similar geometry to those shown in Figure 4 were used by Chan (1990), who related G^* to a non-dimensional film thickness h that is defined as,

$$h = \frac{\delta}{d_2 - d_1}, \qquad (2)$$

where δ is the (dimensional) film thickness. The conductance between the electrodes was calculated by using a CFD code (PHOENICS), which allowed a polynomial relationship between h and G^* to be obtained as follows (to 4 decimal points),

$$h = 0.2379G^* + 0.0400G^{*2} + 0.1286G^{*3} + 0.4547G^{*4}. \qquad (3)$$

In order to confirm this relationship, a number of calibration tests were carried out by placing liquid films of known thickness (by using machined components) and various conductivities (by using water with a varying degree of salt addition) over the sensors. Good agreement was found between the resulting calibration data and the relationship in Equation (3). In the present work, an extended series of further calibration tests were performed in which, having selected the salt concentration in our aqueous solution, liquid films of varying and known thickness where placed over all eight sensors, again by employing a set of precisely machined tube sections and inserts. This series of tests also showed good agreement with Equation (3). Thus, having confirmed the validity of Equation (3), the film thickness calculated from the present data was obtained by estimating G^* from the conductance of the film and then h (and consequently δ) from Equation (3).

An error analysis was also performed with the probes positioned in the vertical tube apparatus at various positions from the inlet. In this set of tests multiple measurements of a series of flow conditions (a combination of a certain gas and liquid flow-rate) were performed by different probes at different positions in the tube, by rotating and/or moving the probe support sections. It was found that the relative standard error of the local mean film thickness , which was estimated by evaluating the standard deviation in the local mean film thickness $\sigma_{\bar{\delta}}$ relative to (i.e. divided by) the overall local mean film thickness $\bar{\delta}$, was ±1-3% at long distances from the inlet (independent of gas and/or liquid flow-rate), ±8-12% at short distances and at low liquid flow-rates, and ±6-9% at short distances and at high liquid flow-rates (within our range of investigated conditions). In our work 7500 samples were taken per probe, per flow condition. For some conditions multiple recordings were made.

As was stated above, four concentric probes were mounted at an equal distance around an acrylic resin body on the same diameter as the tube, which was flanged so that it could be placed at various positions relative to the injector. In addition to the measurements on the liquid film, measurements were also made of the pressure gradient by measuring the pressure difference (using a Rosemount pressure transducer with an accuracy of ±0.1% of full-scale, as

stated by the manufacturer) between two pressure tappings whose position depended on the layout of the test section, but which was typically 0.47 m.

Table 1 shows the experimental conditions investigated in our experiments in terms of the liquid and gas flow-rates and also the corresponding liquid film and gas Reynolds numbers (Re_L and Re_G, respectively) and the distances at which these measurements were made from the inlet (L). The liquid and gas Reynolds numbers are based here on the *bulk* flow speed (i.e. volumetric flow-rate averaged over the *flow* cross-sectional area) in the liquid and gas phases, U_L and U_G respectively, which are defined explicitly in Table 1. The characteristic length scales used in the two definitions are the mean liquid film thickness $\bar{\delta}$ (for Re_L) and the tube internal diameter D (for Re_G). Note that for the gas phase this definition of Re_G is similar to that based on the superficial gas velocity (i.e. volumetric gas flow-rate averaged over the entire tube cross-sectional area, $4Q_G/\pi D^2$) and the tube diameter D, however, for the liquid phase this definition of Re_L is four times *smaller* than that based on the superficial liquid velocity (i.e. volumetric liquid flow-rate averaged over the entire tube cross-sectional area, $4Q_L/\pi D^2$) and the tube diameter D. In all the experiments, the outlet pressure was atmospheric and the liquid temperature was typically close to room temperature (around 25 °C).

3. RESULTS

Even with the restricted matrix shown in Table 1, a large number of experimental data points was generated in the experiments. Examination of the measured data was carried out in two distinct ways. Firstly, the direct film thickness measurements from any probe or combination of probes were plotted as film thickness versus time. These plots provide the full information about the wave structure and its development, and all subsequent analyses are based on these data. Secondly, the instantaneous film thickness data were analysed using statistical analysis methodologies to obtain quantitative information concerning the interfacial structure and its development over the distance from the liquid inlet, L.

The outcomes from the measurements and the above analyses are described in the following three sections, starting in Section 3.1 with the axial development of the mean film thickness in the pipe from a station close to the liquid inlet ($L = 0.15\ D$) to a distance of $L = 58\ D$ from the inlet, proceeding in Section 3.2 to a presentation of the direct measurement data pertaining to the temporal evolution of the film structure over the same length. Finally, in Section 3.3, the results from the statistical analysis of the data contained in Section 3.2 are presented.

3.1. Mean film thickness development

In Section 3.2, results are presented of the temporal evolution of the liquid film thickness normalised by the mean film thickness at the location where a measurement was made. Therefore, in preparation for these results, we consider here the evolution of the mean film thickness in the pipe. Figure 6 shows results for the mean film thickness at various axial stations from the liquid inlet. In particular, the plot in Figure 6(a) was generated for subcritical conditions ($Re_L = 211$), in which disturbance waves are not observed over our investigated condition envelope of $43540 < Re_G < 93300$, while the plot in Figure 6(b) is for conditions with a Re_L value ($Re_L = 603$) above the critical threshold for the same range of gas Reynolds numbers Re_G (see the discussion in Section 3.2 for details). The film thickness

results are shown averaged over the four probes around the pipe circumference at the plane corresponding to each axial station. The mean film thickness and the axial length from the inlet are normalised by the pipe diameter D. It can be seen in this figure that, for a given liquid flow-rate (and hence for a given liquid Reynolds number Re_L), an increase in the gas flow-rate, or Re_G, gives rise to thinner films. The similarity of the observed trends across the flows with different Re_G, which originate from separate experimental runs, suggests that the results are affected negligibly by noise or other experimental uncertainties. In addition, it was also found (though not shown here) that for a given Re_G the mean film thickness increased monotonically with Re_L, as expected from all previous studies of similar flows (e.g. Schubring *et al*. (2010b, 2010c), and others).

In Figure 6, the normalised mean film thickness shows evidence of development up to a length of between $L/D \sim 20$ (for the flow with $Re_L = 211$) and $L/D \sim 25$ (for $Re_L = 603$). It is interesting to note that the liquid flow in the subcritical case accelerates and thins immediately after its introduction at the inlet, whereas the high Re_L equivalent flow slows slightly and thickens. In both cases, prior to becoming fully-developed, the film decelerates initially showing a local maximum in Figure 6, and then accelerates again and becomes thinner. Nevertheless, the changes in the time-averaged film thicknesses with L are generally small; less than 20% at most (for case $Re_L = 603$ and $Re_G = 43540$) and generally within ± 10% of their axially averaged values.

Figure 7 shows results of the dimensionless thickness δ^+, which has been evaluated from,

$$\delta^+ = \frac{\rho_L u^* \bar{\delta}}{\mu_L}, \qquad (4)$$

where ρ_L and μ_L are liquid phase density and dynamic viscosity, respectively, $u^* = (\tau_w/\rho_L)^{1/2}$ is the wall friction velocity defined using the wall shear stress τ_w, and $\bar{\delta}$ is the circumferentially and axially averaged time-mean film thickness at long distances from the inlet (at L/D of 26.7 and 58.0). The wall shear stress τ_w was obtained here from the independent measurements of the pressure gradient $\Delta P/\Delta L$, i.e. $\tau_w = (\Delta P/\Delta L)D/4$. The experimental results are compared with predictions based on a commonly used approximation in annular flow that is referred to as the "triangular relationship" between the time-averaged film thickness, the film (liquid) flow-rate and the mean interfacial shear stress. The interfacial shear stress is obtained here from the measured time-averaged pressure gradient, under the (reasonable) assumption in annular flow that the variation of shear stress within the liquid film in the wall-normal direction is small compared to the value of this interfacial shear stress, such that the wall shear stress is approximately equal to the interfacial shear stress.

The triangular relationship postulates that when any two of the following three variables: liquid flow-rate, mean film thickness, and pressure gradient, are known, then it possible to predict the third one. For the current experiments, the mean film thickness and the pressure gradient have been measured and (for the short distance between the measurement points and the tube entrance) it is reasonable to assume that the liquid lost from the film by droplet entrainment is small and that the film flow-rate is equal to the input liquid rate. The triangular relationship is discussed in detail by Hewitt and Hall-Taylor (1970). Generally, it has been obtained by integrating non-dimensional relationships for the turbulent velocity profile based on measurements in single phase flow (for instance the von Karman universal velocity profile, or the "1/7th power-law" turbulent velocity profile proposed by Taylor). The

relationship between film thickness and film flow-rate for a given pressure gradient is an implicit one and it is particularly convenient to use an explicit form which was derived by Kosky and Staub (1971) from results obtained by integration of the universal velocity profile (see Hewitt *et al*. 1994 for details). The Kosky and Staub relationships are as follows:

$$\delta^+ = \begin{cases} 0.7071 Re_f^{0.5000}; & Re_f \le 50 \\ 0.6323 Re_f^{0.5286}; & 50 < Re_f < 1483 \\ 0.0504 Re_f^{0.8750}; & Re_f \ge 1483 \end{cases} \qquad (5)$$

where the film Reynolds number is given by $Re_f = G_L D/\mu_L$ and G_L is the liquid mass flux referred to the full cross-section of the pipe.

It is evident in Figure 7 that the lowest Re_G test case (Re_G = 43540) is not predicted well by the Kosky and Staub relationship; specifically, it is under-predicted by 20-30%. However, it should be noted that this flow was (by direct observation) on the transition between churn flow and annular flow, when the assumption that the wall shear stress is approximately equal to the interfacial shear stress is no longer as reliable. Neglecting the transitional flow case, the Kosky and Staub relationship in Eq. (5) appears to under-predict the film thickness for lower Re_G and to over-predict slightly the film thickness for higher Re_G. Nevertheless, the agreement is reasonable (within ±6% on average; with a worst case deviation of 13%) given the experimental uncertainty involved (up to ±3% at long lengths; see Section 2) along with the approximate nature of the theoretical analysis that gives rise to the prediction, with the possible exception of flows with the lowest Re_G. Though there is reasonable agreement between predictions and measurements, the agreement is not as good as that observed for fully-developed flows (Hewitt and Hall-Taylor 1970). The subject of proposing relationships for *developing* flows such as those discussed here seems worthy of further investigation.

3.2. Temporal film thickness development

It was stated in the Introduction that the occurrence of disturbance waves is a necessary condition for droplet entrainment in annular flow (at least with low liquid viscosities). There have been a number of attempts to collect data for the liquid film Reynolds number at which disturbance waves/liquid entrainment begins. It has been found that this Reynolds number is independent of the gas velocity, provided the gas velocity is sufficient to have well-established annular flow. A typical correlation for the onset of disturbance waves/entrainment is that of Owen and Hewitt (1986), which is given as,

$$\frac{\dot{m}_{LFC} D}{\mu_L} = Re_{LFC} \approx \exp\left\{5.850 + 0.425 \frac{\mu_G}{\mu_L}\sqrt{\frac{\rho_L}{\rho_G}}\right\}, \qquad (6)$$

where $\dot{m}_{LFC}$ is the critical mass flux of the liquid phase at which disturbance waves/entrainment are initiated, D is the tube diameter and μ_L is the liquid phase dynamic viscosity. Also in Equation (6), μ_G is the gas dynamic viscosity, and ρ_L and ρ_G are the liquid and gas densities respectively. For the present experiments, Equation (6) yields an approximate value of $Re_{LFC} \approx 450$, based on the values $\mu_L = 8.90 \times 10^{-4}$ kg/m.s, $\mu_G = 1.86 \times 10^{-5}$ kg/m.s, $\rho_L = 1.00 \times 10^3$ kg/m^3 and $\rho_G = 1.18$ kg/m^3, all at 25 °C.

It is noted that the above Reynolds number Re_{LFC} is considerably lower than that expected for transition to turbulence in the film in an annulus flow regime in the absence of a turbulent gas core flow. In that flow case, the theoretical analysis of Dou *et al*. (2010) suggests a critical liquid Re_L (equivalent to that employed in this paper) of around 1330, based on the measured mean film thicknesses in our flows. The predictions of Dou *et al*. (2010) have shown good agreement with experimental data taken in annulus flows by Hank and Bonner (1971). On the other hand, the Reynolds number $Re_{LFC} = 450$ is close to the critical value of 380 suggested by Azzopardi (1997) and Alekseenko *et al.* (2009), based on the liquid phase and the geometry of the experiments discussed in the present paper.

Figures 8 and 9 show data for the film thickness as a function of time for liquid Reynolds numbers of 211 and 603, respectively. The data are shown as a function of distance from the injector L and for a fixed circumferential position. As can be seen, the data for the lower Reynolds number of $Re_L = 211$ (Figure 8) showed no particular change with axial distance and there is an absence of the high peaks in amplitude characteristic of disturbance waves. Figure 9, on the other hand, indicates how the disturbance waves are generated as a function of distance, for the high Reynolds number case ($Re_L = 603$). Initially, the film is covered with ripples but these evolve into the larger waves and the disturbance waves are seen very clearly at the longest distance observed ($L = 2.0$ m from the inlet, corresponding to a tube length to diameter ratio of $L/D = 58$). It will also be shown in Section 3.3 that the overall wave frequency is decreasing with length, possibly due to the coalescence of smaller amplitude waves leading to disturbance wave growth as suggested first by Hall-Taylor and Nedderman (1969). Further analyses of wave frequency are reported in Section 3.3 below.

The main new information reported here is on the circumferential evolution of the disturbance waves. In Figures 10 to 14 results are also shown for the simultaneous recording of time-averaged film thickness from the four probes equally spaced around the circumference at a given distance from the liquid inlet. The distances were, respectively, $L = 0.15$ m ($L/D = 4.3$) from the inlet injector (Figure 10), $L = 0.26$ m ($L/D = 7.5$) from the inlet injector (Figure 11), $L = 0.62$ m ($L/D = 18.0$) from the inlet (Figure 12), $L = 0.92$ m ($L/D = 26.7$) from the inlet (Figure 13), and $L = 2.0$ m ($L/D = 58.0$) from the inlet (Figure 14). This set of results corresponds to Reynolds numbers of $Re_L = 603$ and $Re_G = 93300$. Figure 10 (just above the injector) shows somewhat random small-amplitude wave structures, with the waves at each circumferential location not noticeably correlated. The wave structure develops along the channel and the emergence of the sharply peaked wave characteristic of disturbance waves is clearly seen and the coherence of these waves around the tube periphery gradually develops. This coherence becomes very clear in Figure 14 ($L/D = 58.0$ from the inlet).

One may conclude from the sequence of results contained in Figures 10 to 14 that structures occur at specific circumferential locations and spread around the periphery to make coherent disturbance waves which are fully-developed and well-characterised by a distance of $L/D = 58.0$ from the injector. Further analysis of these data to obtain a quantitative estimate of the manner in which the correlation develops is presented in Section 3.3 below.

3.3. Statistical analysis

The signals from the conductance probes can be analysed statistically in various ways which can throw further light on the wave development processes illustrated qualitatively in

Section 3.2. An obvious quantity for our investigation is that of interfacial wave frequency. This has been obtained in two ways: (i) by carrying out a power spectral density (PSD) analysis on the signals (Section 3.3.1); and (ii) by counting instances of "large waves" (defined as having a thickness of 1.6 times the mean thickness, or more) passing the measurement location (Section 3.3.2). Furthermore, we have defined a quantitative measure of the "ring-like" wave coherence developing around the periphery, via the evaluations of circumferential correlation coefficients between pairs of probes on the same axial plane, at the same downstream distance from injection (Section 3.3.3).

3.3.1 Interfacial wave spectral density

The power spectral density (PSD) procedure on the film thickness signals was implemented using standard MATLAB functions, and typical results from this analysis are shown in Figure 15. In this figure a series of plots are given for a selected flow condition ($Re_L = 603$, $Re_G = 93300$) at the same circumferential location. The peak frequency decreases gradually with increasing distance from the inlet, as the waves develop.

Data for the peak frequency (f_{PP}) obtained from plots such as those shown in Figure 15 are shown in Figure 16 as a function of axial distance L/D. The points appearing in Figure 16 are averaged over the four probes that were at the same particular axial location. This graph is analogous to that obtained by Hall-Taylor and Nedderman (1969) at a single position around the tube periphery, which was illustrated earlier in Figure 1. Ultimately, from a distance from the inlet of about $L/D \sim 20$ this frequency measure becomes essentially independent of distance, indicating that the waves have become fully-developed in this regard.

Nevertheless, although the frequency measure f_{PP} from the PSDs attains a constant value from a distance of $L/D \sim 20$, it is interesting to mention here that:

(1) The disturbance waves actually become increasingly rare beyond this distance (see Figure 17); while,
(2) The circumferential coherence of the disturbance waves continues to increase beyond this distance (see Figure 24).

The results concerning the disturbance wave frequency from direct large wave counting, and the circumferential coherence of the disturbance waves are reported in the following sections (Section 3.3.2 and Section 3.3.3, respectively).

The first observation, in Point (1) above, suggests that the consideration of the frequency of the peaks in the PSD plots, which has been the conventional means for the identification of disturbance waves (e.g. in the extensive effort by Azzopardi 1997), may not by the most reliable method for this task. In fact, the decreasing disturbance wave frequency leads naturally to a reduction in the relative contribution of the large waves towards the overall frequency content of the wave signals and hence the PSDs that are reported here in Figure 15; note that the spectral signatures reported by these PSDs correspond to the full wave content, covering the full range from small-amplitude to large-amplitude waves, and not only to disturbance waves. Furthermore, the two observations in Points (1) and (2) when taken together suggest that the disturbance waves continue to evolve beyond $L/D \sim 20$, in a way that would be consistent with wave coalescence. As with the disturbance wave frequency, this information is lost when considering only the peaks from the PSDs.

3.3.2 Large amplitude wave counting

In an effort to generate information specifically and exclusively on the disturbance waves, an in-house, dedicated MATLAB script was developed to count waves with large amplitudes (defined in this work as having amplitudes 1.6 times the mean film thickness or more) from wave time traces such as those shown in Figures 10 to 14. The choice of the factor was to some extent arbitrary, since it was confirmed that the results were not sensitive to this choice within a suitable range; a higher value identifying fewer, higher-amplitude waves, but with the overall trends being similar. A range of factors between 1.5 and 1.7 were tested, and the value of 1.6 was selected as a good compromise. The data were then averaged over the four probes that were at the same axial location and the results are shown in Figure 17.

Here it can be seen that the frequency of occurrence of the disturbance waves (f_{lw}) and peak frequency f_{PP} obtained from PSD plots (and reported above in Figure 16) are of the same order of magnitude, but do not follow the same trend and can differ by a factor of up to ~5 at the lower Re_G and higher L/D. The disturbance wave frequency f_{lw} first increases away from the inlet, reaches a maximum and then decreases again. Generally the frequency of disturbance waves increases at higher Re_G (and Re_L), in line with the overall interfacial wave frequency content f_{PP} presented in Figure 16 and discussed in the preceding section. The maximum appears at a length between 7.5 and 15 pipe diameters from the inlet, and appears to move upstream and closer to the injector at progressively higher Re_G.

The rise of f_{lw} close to the injector is clearly a reflection of the early development of these waves, which initially have considerably lower amplitudes compared to their eventual values. The drop of f_{lw} far away from the injector may be due to wave coalescence, or equivalently due to wave break-up leading to liquid entrainment into the gas core in the form of droplets (Andreussi 1983; Azzopardi 1997; Pan and Hanratty 2002; Sawant *et al*. 2008a), which would result in the annihilation of these waves. Both of these mechanisms would lead to a decrease in the frequency of large waves; coalescence, however, would lead to an increase, whereas break-up and entrainment would lead to a decrease in the large wave amplitudes.

3.3.3 Circumferential film thickness correlation

The correlation developing around the pipe periphery as observed visually in Figures 10 to 14 can be expressed in quantitative form by defining a cross-correlation function as follows:

$$R_{xy}(m) = \begin{cases} \sum_{n=0}^{N-m-1} x_{n+m} y_n^* \; ; & m \geq 0 \\ R_{xy}(-m) \; ; & m < 0 \end{cases} \qquad (7)$$

The cross-correlation function was determined quantitatively from the data by the application of a built-in routine in MATLAB. Typical results for the cross-correlation function are shown in Figure 18, where the function is evaluated over a range of time differences Δt between two probes *opposite each other* at the same axial location. The data were obtained for $Re_L = 603$ and $Re_G = 93300$. The two signals at $L/D = 4.3$ from the injector are uncorrelated, but the same probes show a strong correlation at a far distance of $L/D = 58.0$.

It is also interesting to consider the correlations between *adjacent* probes. A set of results illustrating this development is shown in Figures 19 to 23. Here, correlations between adjacent probes (1&3, 2&4, 1&4, 2&3, 6&8, 5&7, 6&7 and 5&8) are shown for the flow with conditions $Re_L = 603$ and $Re_G = 93300$. The respective graphs at any one position are the

cross-correlation functions between adjacent probes (the probes being separated by 90° around the tube periphery at a given axial distance from the inlet). At a distance of $L/D = 4.3$ from the injector, Probes 1 and 2 and Probes 3 and 4 begin to show a weak, but definite cross-correlation peak at zero delay, which signifies a correlated ring passing as a coherent structure over the four probes. As one proceeds up the pipe, the correlation strengthens and the peak value of the cross-correlation function increases in magnitude until, eventually, at a distance of $L/D = 58.0$ from the injector (Figure 23) there is a strong correlation between each probe pair. It would thus seem that the disturbance waves begin to grow at some point on the periphery relatively close to the injector and that the waves then spread to cover the whole of the circumference of the tube at a distance of around $L/D = 58.0$.

The peak magnitude in the cross-correlation function at zero delay can be plotted as a function of normalised distance from the inlet; this is done in Figure 24. A high value of this parameter would signify a correlated ring passing as a coherent structure over the four probes. It can be seen that the cross-correlation magnitude increases gradually with distance as might be expected. Thus, it would seem that the correlation of the signals, a key characteristic of coherent "ring-like" disturbance waves, is established gradually over a distance of around 1 to 2 metres (or, 30 – 60 pipe diameters) from the inlet. The coherence appears from lengths of about 5 – 10 pipe diameters and gradually strengthens with increasing distance from the inlet.

Finally, the peak magnitude in the cross-correlation function at zero delay is plotted at the same distance from the inlet as a function of Re_G in Figure 25, for two flows with: (a) a subcritical $Re_L = 211$ when no disturbance waves are observed; and (b) $Re_L = 603$. Clearly, the cross-correlation coefficient magnitudes are low at subcritical conditions, signifying a lack of circumferential coherence. On the other hand, at $Re_L = 603$ the cross-correlation coefficient shows significant values that increase with L/D. The maximum cross-correlation coefficient at a given L/D decreases monotonically with increasing Re_G close to the injector, but shows a more complex relationship at longer L/D. From $L/D = 17.4$ onwards a turning point develops. As Re_G is increased from low values, the cross-correlation coefficient magnitudes increases, reaches a maximum and then decreases again. This provides added evidence to support the idea that not only is the initiation, but also possibly the annihilation of the disturbance waves is linked directly to the turbulence levels in the gas core (i.e. there is a level of turbulence in the gas that can act to break up the disturbance waves leading to entrainment, and this level must be higher the larger and more coherent these waves are, which is what is found further downstream). This idea is also in agreement with the knowledge that entrainment strongly increases at progressively higher Re_G, within our range of investigated conditions (see e.g. Sawant *et al*. (2008a), and refer to Table 1). A further investigation is necessary to study this more closely.

4. CONCLUSIONS

This paper reports on new measurements on the development of disturbance waves in annular flow. The following main conclusions are drawn:

(1) The measurements confirm that disturbance waves do not grow at liquid film Reynolds numbers less than a critical value. If the Reynolds number exceeds this critical value, then disturbance waves are observed.

(2) In the region where disturbance waves are created, such waves become coherent around the periphery of the tube, with the waves forming the ring-like structures that has been reported in the past by, for instance by Hewitt and Lovegrove (1969). However, these ring-like structures are not created instantaneously but, rather, grow gradually from wavy initiation at a given circumferential position that is as short as 5 – 10 pipe diameters from the liquid inlet, and spread around the periphery to exhibit a much stronger circumferential coherence farther downstream.

(3) In the disturbance wave region, the overall frequency content of the interfacial waves (as determined by using analysis of the film thickness versus time data using power spectral density analysis) decreases with increasing length in the first 20 pipe diameters as previously observed by Hall-Taylor and Nedderman (1969), but then seems to reach a plateau. This decrease in wave frequency probably occurs (as suggested by Hall-Taylor and Nedderman (1969)) due to the coalescence of waves, and this coalescence process occurs simultaneously with the development of circumferential coherence in the waves.

(4) This coalescence, and possibly the break-up of large waves leading to liquid droplet entrainment into the gas core, also gives rise to fewer disturbance waves at longer distances from the inlet. Thus, the frequency of occurrence of disturbance waves increases early on as these waves begin to form, reaches a maximum at a length between 7.5 and 15 pipe diameters from the inlet that depends on the flow conditions (this maximum shifts gradually towards the injector with increasing gas Reynolds number), and then decreases again as the coalescence/break-up processes progress.

The measurements reported here fill in a surprising gap in our knowledge of disturbance wave creation and behaviour. To the authors' knowledge, this is the first time that the growth of circumferential coherence has been quantitatively explored.

The disturbance wave phenomenon is a vital one in annular flow and, based on the findings reported in the present paper, further studies of this phenomenon are recommended and are being pursued. Experimentally, further detailed measurements on the development of disturbance waves are recommended, including:

(1) More accurate measurements of film thickness at some azimuthal position around the pipe circumference, using a fluorescence method (see the original work of Hewitt and Nicholls (1969), and the more recent efforts by Alekseenko *et al.* (2009), Schubring *et al.* (2010b, 2010c), Farias *et al*. (2012), Morgan *et al*. (2012a, 2012b), and Zadrazil *et al*. (2012)), or an equivalent technique, which would allow for a more accurate measurement of the peak amplitudes of the complex interfacial waves.

(2) Using micro-PIV techniques, such as that used by Schubring *et al.* (2009), it may be possible to determine the development of turbulent structures within the waves.

In addition to these possible lines of further experimental investigation, the possibility of numerical modelling of disturbance wave initiation and development should also be borne in mind (though it has not so far been within the compass of feasible numerical calculations).

References

Alekseenko, S.V., Nakoryakov, V.E. and Pokusaev, B.G., 1994. Wave Flow of Liquid Films. Begell House, New York.

Alekseenko, S.V., Antipin, V., Cherdantsev, A., Kharlamov, S. and Markovich, D., 2009. Two-wave structure of liquid film and wave interrelation in annular gas-liquid flow with and without entrainment, Phys. Fluids 21, 061701.

Ambrosini, W., Andreussi, P. and Azzopardi, B.J., 1991. A physically based correlation for drop size in annular flow, Int. J. Multiphase Flow 17, 497–507.

Andreussi, P, 1983. Droplet transfer in two-phase annular flow, Int. J. Multiphase Flow 9, 697–713.

Andreussi, P., Asali, J.C. and Hanratty, T.J., 1985. Initiation of roll waves in gas-liquid flows, AIChE J. 31, 119–126.

Asali, J.C., Hanratty, T.J. and Andreussi, P., 1985. Interfacial drag and film height for vertical annular flow, AIChE J. 31, 895–902.

Azzopardi, B.J., 1986. Disturbance wave frequency, velocities and spacing in vertical annular two-phase flow, Nucl. Eng. Design 92, 121–133.

Azzopardi, B.J., 1997. Drops in annular two-phase flow, Int. J. Multiphase Flow 23, 1–53.

Belt, R.J., van't Westende, J.M.C. and Portela, L.M., 2009. Prediction of the interfacial shear-stress in vertical annular flow, Int. J. Multiphase Flow 35, 689–697.

Cousin, L.B., Denton, W.H. and Hewitt, G.F., 1965. Liquid mass transfer in annular two-phase flow, UKAEA AERE-R4926.

Cousin, L.B, Denton, W.H. and Hewitt, G.F., 1965. Liquid phase mass transfer in annular two-phase flow: Droplet deposition & liquid entrainment, UKAEA AERE-R5657.

Dou, H.-S., Khoo, B.C. and Tsai, H.M., 2010. Determining the critical condition for turbulent transition in a full-developed annulus flow, J. Petroleum Sci. Eng. 73, 41–47.

Dukler, A.E., Smith, L. and Chopra, A., 1984. Flooding and upward film flow in tubes–I. Experimental studies, Int. J. Multiphase Flow 10, 585–597.

Farias, P.S.C., Martins, F.J.W.A., Sampaio, L.E.B., Serfaty, R. and Azevedo, L.F.A., 2012. Liquid film characterization in horizontal, annular, two-phase, gas–liquid flow using time-resolved laser-induced fluorescence, Exp. Fluids 52, 633–645.

Fore, L.B., Beus, S.G. and Bauer, R.C., 2000. Interfacial friction in gas-liquid annular flow: Analogies to full and transition roughness, Int. J. Multiphase Flow 26, 1755–1769.

Fukano, T. and Furukawa, T., 1998. Prediction of the effects of liquid viscosity on interfacial shear stress and frictional pressure drop in vertical upwards gas-liquid annular flow, Int. J. Multiphase Flow 24, 587–603.

Govan, A.H., Hewitt, G.F., Richter, H.J. and Scott, A., 1991. Flooding and churn flow in vertical pipes, Int. J. Multiphase Flow 17, 27–44.

Hall-Taylor, N.S., Hewitt, G.F. and Lacey, P.M.C., 1963. The motion and frequency of large disturbance waves in annular two-phase flow of air-water mixtures, Chem. Eng. Sci.18, 537–552.

Hall-Taylor, N.S. and Nedderman, R.M., 1968. The coalescence of disturbance waves in annular two phase flow, Chem. Eng. Sci. 23, 551–564.

Han, H., Zhu, Z. and Gabriel, K., 2006. A study on the effect of gas flow-rate on the wave characteristics in two-phase gas-liquid annular flow, Nuclear Eng. Des. 236, 2580–2588.

Hank, R.W. and Bonner, W.F., 1971. Transitional flow phenomena in concentric annuli, Ind. Eng. Chem. Fundam. 10, 105–113.

Hewitt, G.F., 1968. Burnout and Beyond, Engineering and boiler house review 5, 170–174.

Hewitt, G.F., 1982. Handbook of Multiphase Flow (Ed. Hetsroni, G.), Liquid-gas systems, Chapter 10. McGraw-Hill, New York.

Hewitt, G.F. and Hall-Taylor, N.S., 1970. Annular Two-Phase Flow. Pergamon Press, Oxford, UK.

Hewitt, G.F., Lovegrove, P.C. and Nicholls, B., 1964. Film thickness measurements using a fluorescence technique, UKAEA AERE-R4478.

Hewitt, G.F. and Nicholls, B., 1969. Film thickness measurement in annular two-phase flow using a fluorescence spectrometer technique, Part II: Studies of the shape of disturbance waves, UKAEA AERE-R4506.

Hewitt, G.F. and Roberts, D.N., 1969. Investigation of interfacial phenomena in annular two-phase flow by means of the axial view technique, UKAEA AERE-R6070.

Hewitt, G.F., Shires, G.L. and Bott, T.R., 1994. Process Heat Transfer. CRC Press, Boca Raton.

Hurlburt, E.T. and Newell, T.A, 2000. Prediction of the circumferential film thickness distribution in horizontal annular gas-liquid flow, J. Fluids Eng. 122, 396–402.

Jayanti, S. and Hewitt, G.F., 1997. Hydrodynamics and heat transfer in wavy annular gas-liquid flow: a computational fluid dynamics study, Int. J. Heat Mass Transf. 40, 2445–2460.

Jayanti, S., Kandlbinder, T. and Hewitt, G.F., 1996. Turbulent flow in a pipe with intermittent rough patches: An analogue of annular two-phase flow, Chem. Eng. Comm. 141–142, 237–259.

Kaji, R. and Azzopardi, B.J., 2010. The effect of pipe diameter on the structure of gas/liquid flow in vertical pipes, Int. J. Multiphase Flow 36, 303–313.

Kosky, P.G. and Staub, F.W., 1971. Local condensing heat transfer coefficients in the annular flow regime, AIChE J. 17, 1037–1043.

McNeil, D.A. and Stuart, A.D., 2003. The effects of a highly viscous liquid phase on vertically upward two-phase flow in a pipe, Int. J. Multiphase Flow 29, 1523–1549.

McQuillan, K.W. and Whalley, P. B., 1985. A comparison between flooding correlations and experimental flooding data for gas liquid flow in vertical circular tubes, Chem. Eng. Sci. 40, 1425–1440.

Martin, C.J., 1983. Annular Two-Phase Flow, PhD Thesis. University of Oxford, Oxford, UK.

Martin, C.J. and Azzopardi, J., 1985. Waves in Vertical Annular Flow, Physicochemical Hydrodynamics 6, 257–265. Pergamon Press, Oxford.

Morgan, R.G., Markides, C.N., Hale, C.P. and Hewitt, G.F., 2012. Horizontal liquid–liquid flow characteristics at low superficial velocities using laser-induced fluorescence, Int. J. Multiphase Flow 43, 101–117.

Morgan, R.G., Markides, C.N., Zadrazil, I. and Hewitt, G.F., 2012. Characteristics of horizontal liquid – liquid flows in a circular pipe using simultaneous high-speed laser-induced fluorescence and particle velocimetry, Int. J. Multiphase Flow, *accepted*.

Okawa, T., Goto, T. and Yamagoe, Y., 2010. Liquid film behaviour in annular two phase flow under full oscillation conditions. Int. J. Heat Mass Transf. 53, 961–971.

Owen, D.G. and Hewitt, G.F., 1986. A proposed entrainment correlation, UKAEA AERE-R12279.

Pan, L. and Hanratty, T.J., 2002. Correlation of entrainment for annular flow in vertical pipes, Int. J. Multiphase Flow 28, 363–384.

Park, C.D., Nosoko, T., Gima, S. and Ro, S.T., 2004. Wave-augmented mass transfer in a liquid film falling inside a vertical tube, Int. J. Heat Mass Transf. 47, 2587–2598.

Sawant, P., Ishii, M. and Mori, M., 2008. Droplet entrainment correlation in vertical upward co-current annular two-phase flow, Nuclear Eng. Des. 238, 1342–1352.

Sawant, P., Ishii, N., Hazuku, T., Takamasa, T. and Mori, M., 2008. Properties of disturbance waves in vertical annular two-phase flow, Nuclear Eng. Des. 238, 3528–3541.

Schadel, S.A., Leman, G.W., Binder, J.L. and Hanratty, T.J., 1990. Rates of atomization and deposition in vertical annular flow, Int. J. Multiphase Flow 16, 363–374.

Schubring, D., Foster, R.E., Rodríguez, D.J. and Shedd, T.A., 2009. Two-zone analysis of wavy two-phase flow using micro-particle image velocimetry (micro-PIV), Meas. Sci. Technology 20, 065401/1–11.

Schubring, D., Shedd, T.A. and Hurlburt, E.T., 2010. Studying disturbance waves in vertical annular flow with high speed video, Int. J. Multiphase Flow 36, 385–396.

Schubring, D., Ashwood, A.C., Shedd, T.A. and Hurlburt, E.T., 2010. Planar laser-induced fluorescence (PLIF) measurements of liquid film thickness in annular flow. Part I: Methods and data, Int. J. Multiphase Flow 36, 815–824.

Schubring, D., Shedd, T.A. and Hurlburt, E.T., 2010. Planar laser-induced fluorescence (PLIF) measurements of liquid film thickness in annular flow. Part II: Analysis and comparison to models, Int. J. Multiphase Flow 36, 825–835.

Sekoguchi, K., Takashi, U. and Osamu, T., 1985. An investigation of the flow characteristics in the disturbance region of annular flow: Second report on correlation of principle flow parameters. Trans. Japan Soc. Mech. Eng. B51, 1798–1806.

Sekoguchi, K. and Takeishi, M., 1989. Interfacial structure in upward huge wave flow and annular regimes. Int. J. Multiphase Flow 15, 295–305.

Usui, K., 1989. Vertically downward two-phase flow, II: Flow regime transition criteria, J. Nuclear Sci. Tech. 26, 1013–1022.

Wallis, G.B., 1969. One-Dimensional Two-Phase Flow. McGraw-Hill, New York.

Wang, Z., Gabriel, K.S. and Manz, D.L., 2004. The influences of wave height on interfacial friction in annular gas-liquid flow under normal and micro gravity conditions, Int. J. Multiphase Flow 30, 1193–1214.

Wang, Z. and Gabriel, K.S., 2005. The influence of film structure on the interfacial friction in annular two-phase flow under microgravity and normal gravity conditions, Microgravity Sci. Tech. 16, 264–268.

Wongwises, S. and Kongkiatwanitch, W., 2001. Interfacial friction factor in vertical upwards gas-liquid annular two-phase flow, Int. Comm. Heat Mass Trans. 28, 323–336.

Zadrazil, I. Markides, C.N., Matar, O.K., Ó Náraigh, L. and Hewitt, G.F., 2012. Characterisation of downwards co-current gas-liquid annular flows. Proc. 7th Int. Symp. Turb. Heat Mass Transf. (THMT'12), Palermo, Italy.

Table

Table 1: Matrix of investigated experimental conditions at various distances from the inlet where the probes where positioned. The pipe diameter is D = 34.5 mm.

Measurement distances from the inlet L (m)						
0.15	0.26	0.43	0.62	0.71	0.92	2.00
Dimensionless measurement distances from the inlet L/D (-)						
4.3	7.5	12.5	18.0	20.6	26.7	58.0
Matrix of investigated experimental conditions						
Q_L (L/min)	0.35	0.50	0.75	1.00	-	
$Re_L = \rho_L U_L \bar{\delta} / \mu_L$ [$= \rho_L Q_L / \pi D \mu_L$; and $U_L = Q_L / \pi D \bar{\delta}$ (m/s)]	211	302	452	603	-	
Q_G (L/min)	1050	1350	1650	1950	2250	
$U_G = 4Q_G / \pi D^2$ (m/s)	18.7	24.1	29.4	34.8	40.1	
$Re_G = \rho_G U_G D / \mu_G$ [$= 4\rho_G Q_G / \pi D \mu_G$]	43.5×10^3	56.0×10^3	68.4×10^3	80.9×10^3	93.3×10^3	

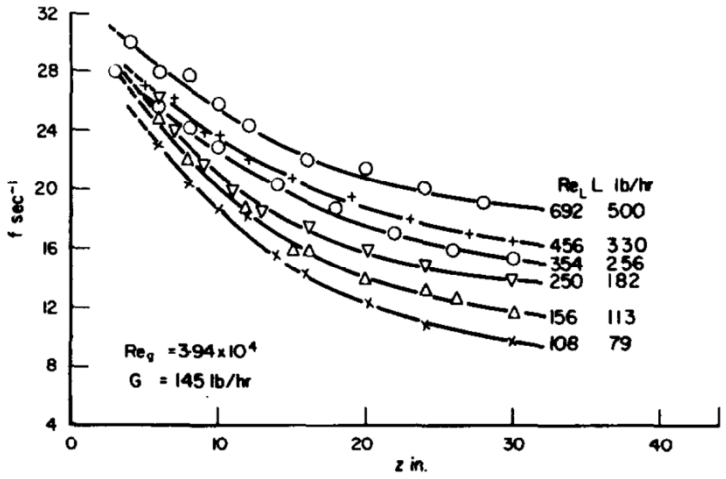
32
28
24
20
16
12
8
4
f sec⁻¹
0
10
20
30
40
z in.
Re_L L lb/hr
692 500
456 330
354 256
250 182
156 113
108 79
Re_g = 3.94 x 10⁴
G = 145 lb/hr

Figure 1

Figure 2

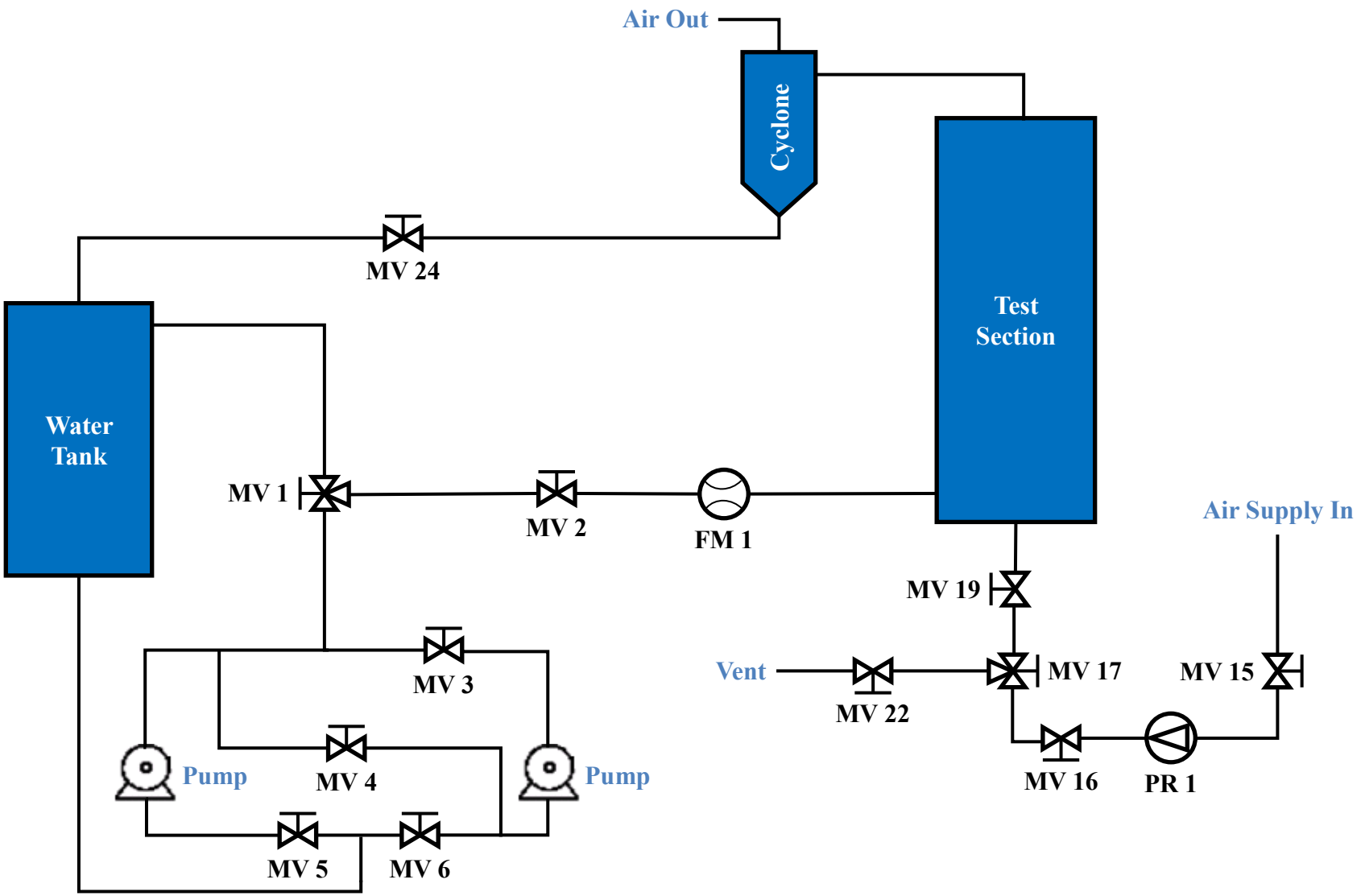

Figure 2

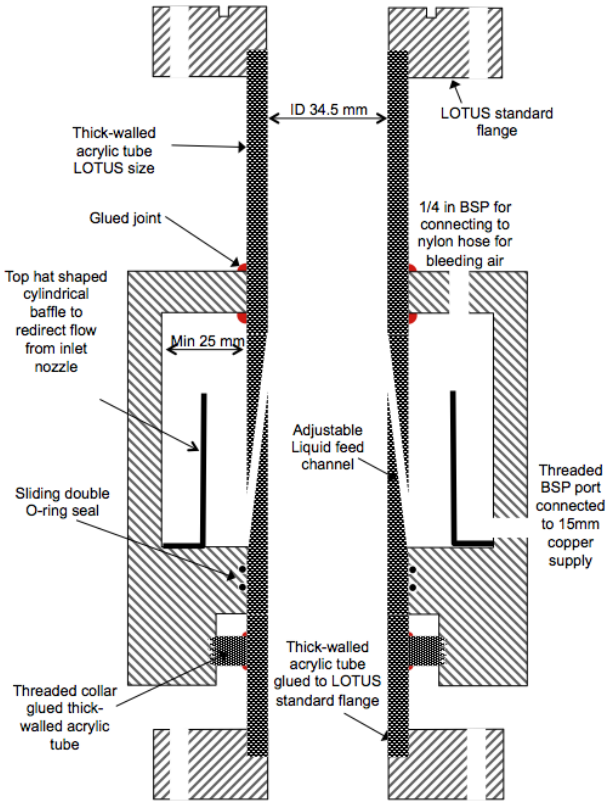
ID 34.5 mm
LOTUS standard flange
Thick-walled acrylic tube LOTUS size
Glued joint
1/4 in BSP for connecting to nylon hose for bleeding air
Top hat shaped cylindrical baffle to redirect flow from inlet nozzle
Min 25 mm
Adjustable Liquid feed channel
Threaded BSP port connected to 15mm copper supply
Sliding double O-ring seal
Thick-walled acrylic tube glued to LOTUS standard flange
Threaded collar glued thick-walled acrylic tube

Figure 3

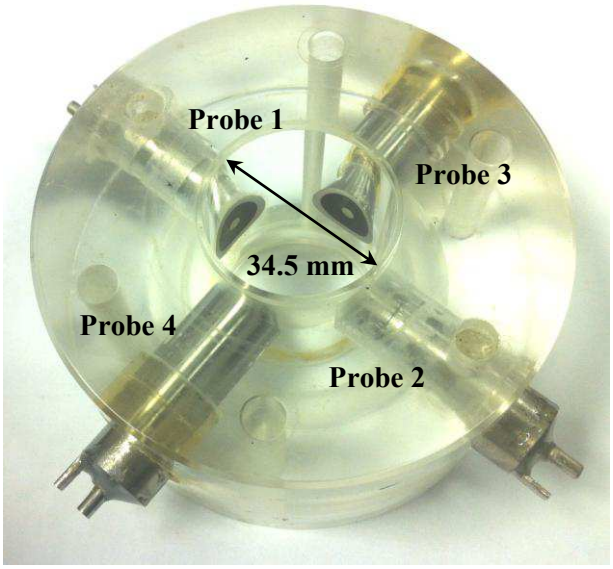

Figure 4

Figure 5

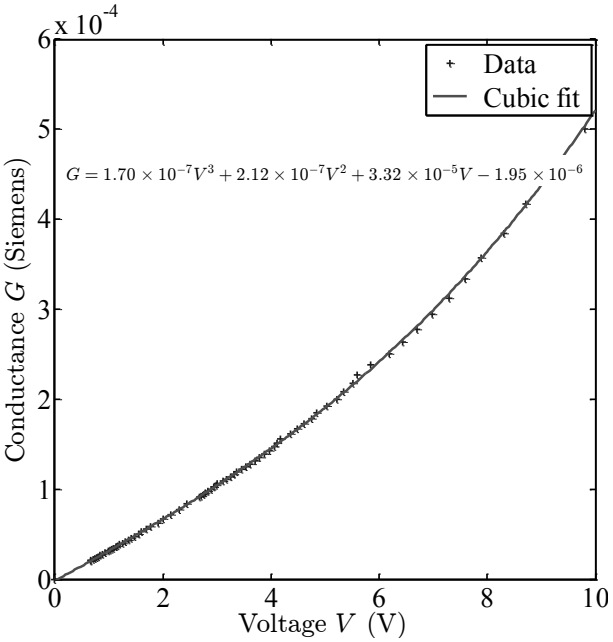

Figure 5

Figure 6

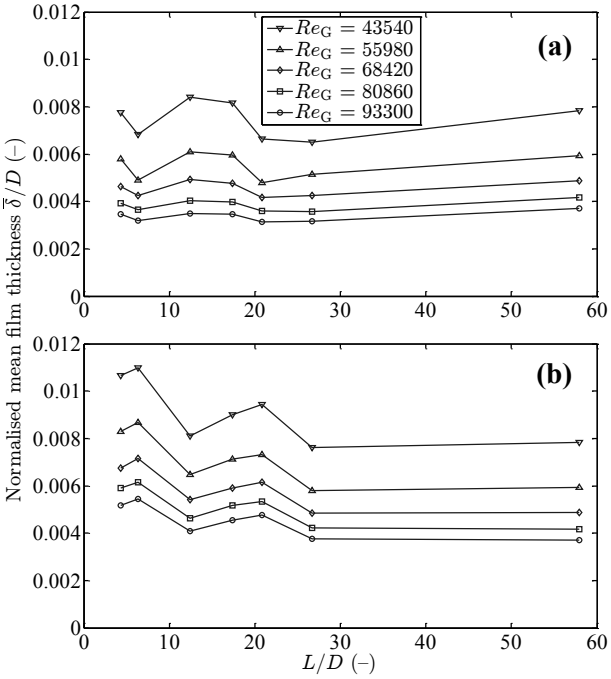

Figure 6

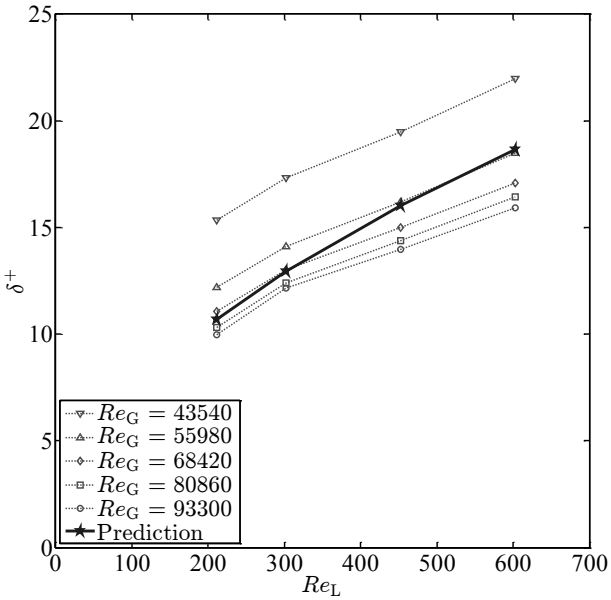
25
20
15
10
5
0
δ^+
0
100
200
300
400
500
600
700
Re_{L}
$Re_{\mathrm{G}} = 43540$
$Re_{\mathrm{G}} = 55980$
$Re_{\mathrm{G}} = 68420$
$Re_{\mathrm{G}} = 80860$
$Re_{\mathrm{G}} = 93300$
Prediction

Figure 7

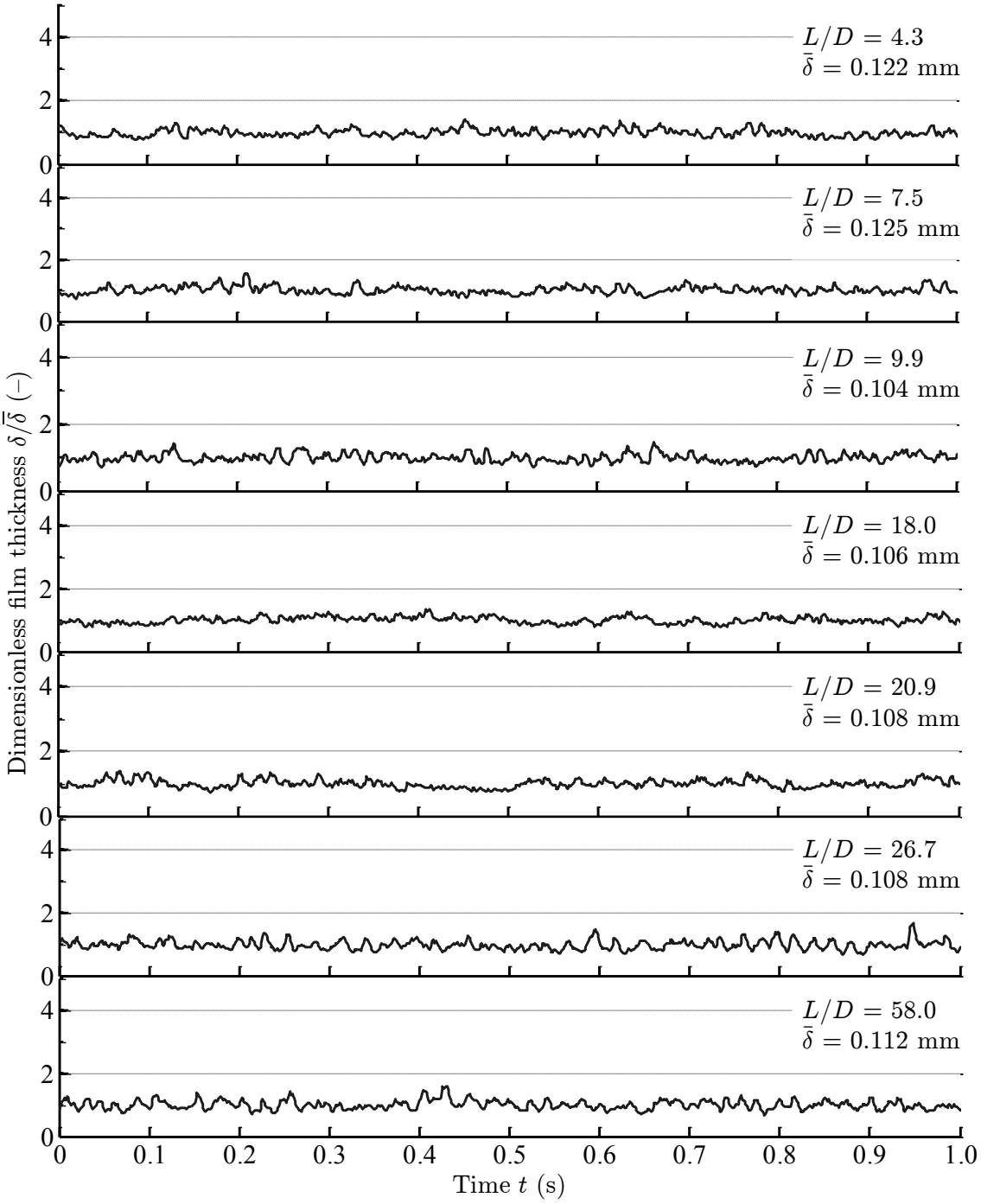
$L/D = 4.3$
$\bar{\delta} = 0.122$ mm
$L/D = 7.5$
$\bar{\delta} = 0.125$ mm
$L/D = 9.9$
$\bar{\delta} = 0.104$ mm
$L/D = 18.0$
$\bar{\delta} = 0.106$ mm
$L/D = 20.9$
$\bar{\delta} = 0.108$ mm
$L/D = 26.7$
$\bar{\delta} = 0.108$ mm
$L/D = 58.0$
$\bar{\delta} = 0.112$ mm
Dimensionless film thickness $\delta/\bar{\delta}$ (–)
Time t (s)

Figure 8

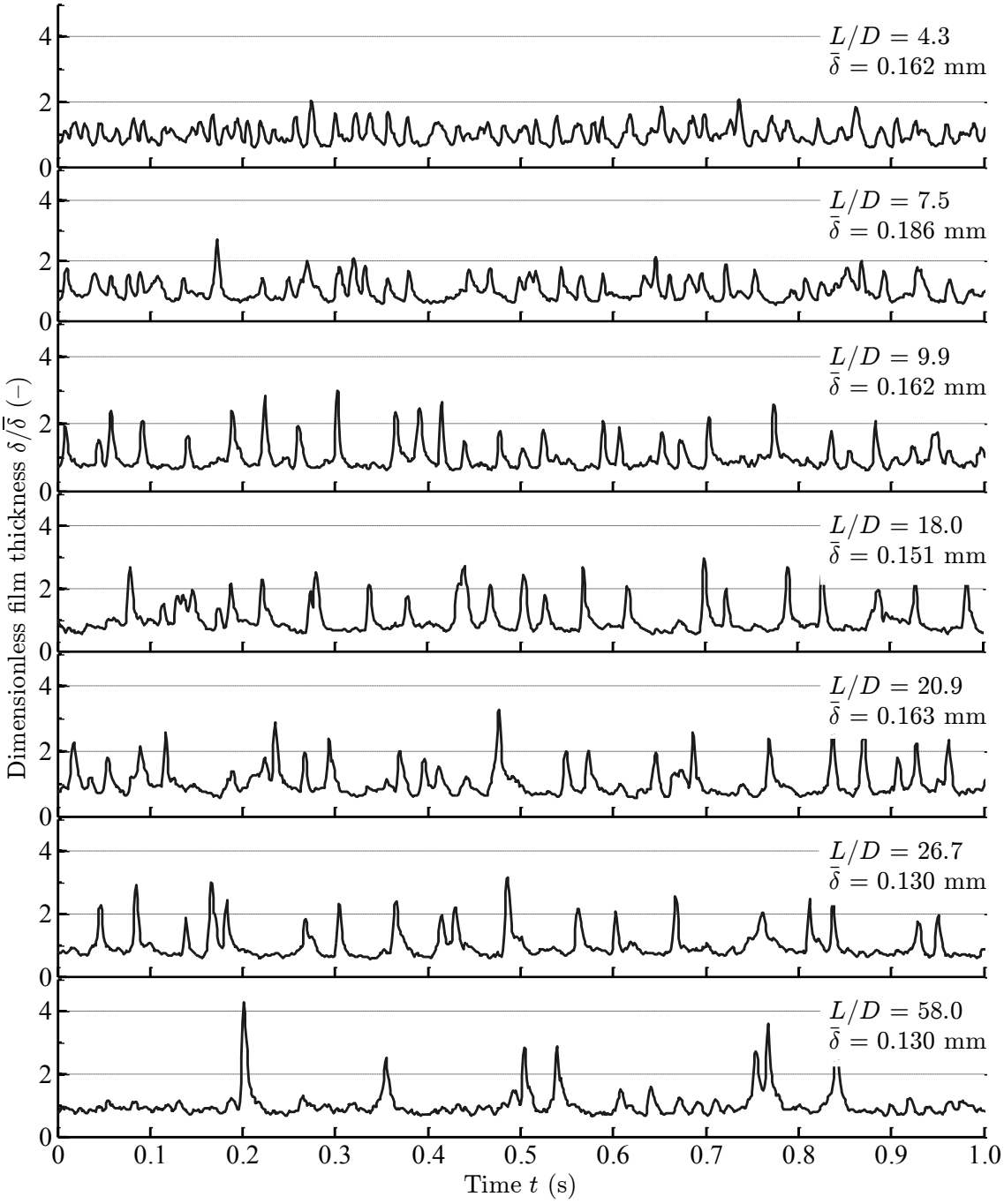
$L/D = 4.3$
$\overline{\delta} = 0.162$ mm
$L/D = 7.5$
$\overline{\delta} = 0.186$ mm
$L/D = 9.9$
$\overline{\delta} = 0.162$ mm
$L/D = 18.0$
$\overline{\delta} = 0.151$ mm
$L/D = 20.9$
$\overline{\delta} = 0.163$ mm
$L/D = 26.7$
$\overline{\delta} = 0.130$ mm
$L/D = 58.0$
$\overline{\delta} = 0.130$ mm
Dimensionless film thickness $\delta/\overline{\delta}$ (–)
Time t (s)

Figure 9

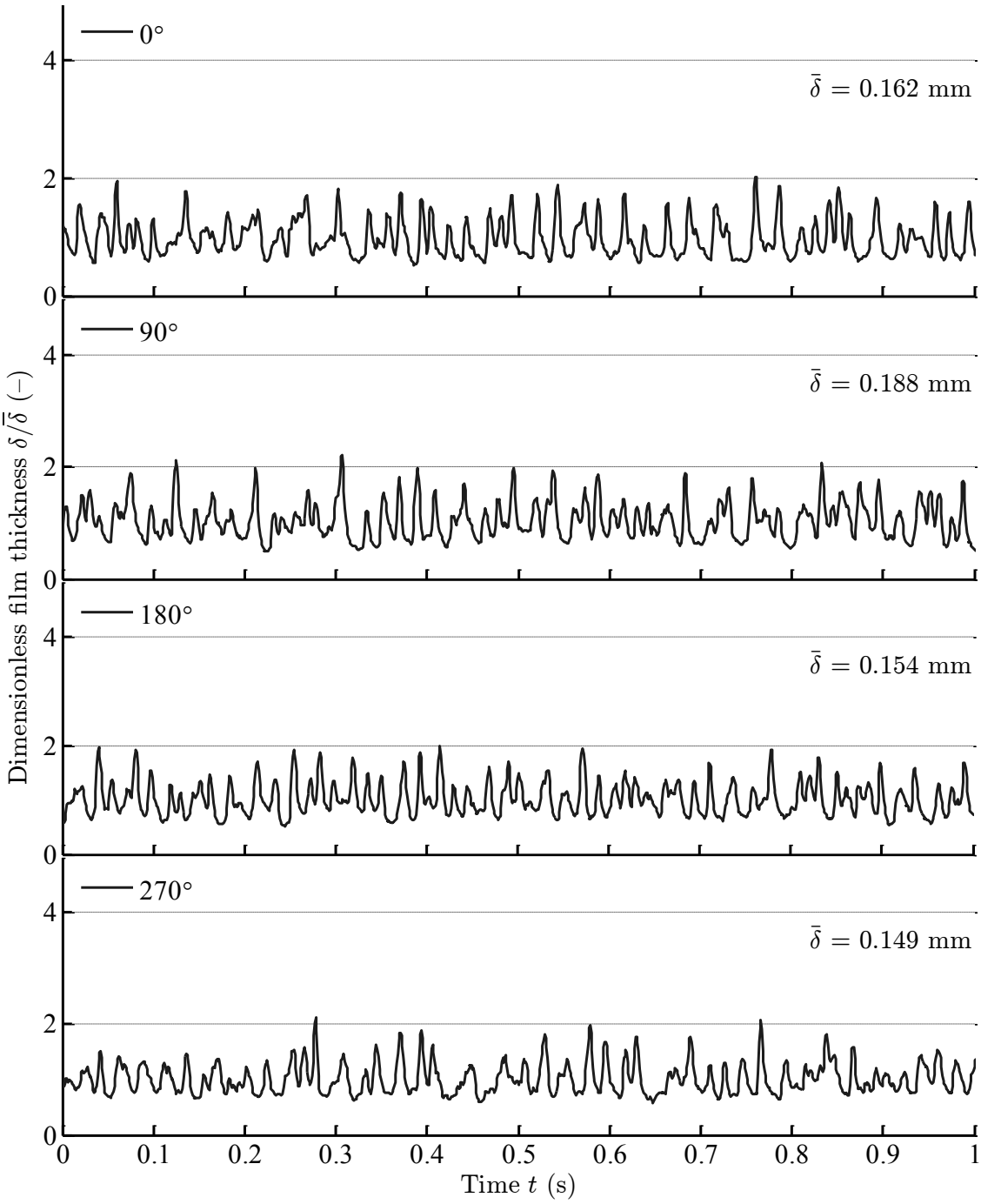
0°
$\bar{\delta}$ = 0.162 mm
90°
$\bar{\delta}$ = 0.188 mm
180°
$\bar{\delta}$ = 0.154 mm
270°
$\bar{\delta}$ = 0.149 mm
Dimensionless film thickness $\delta/\bar{\delta}$ (–)
Time t (s)
0
2
4
0.1
0.2
0.3
0.4
0.5
0.6
0.7
0.8
0.9
1

Figure 10

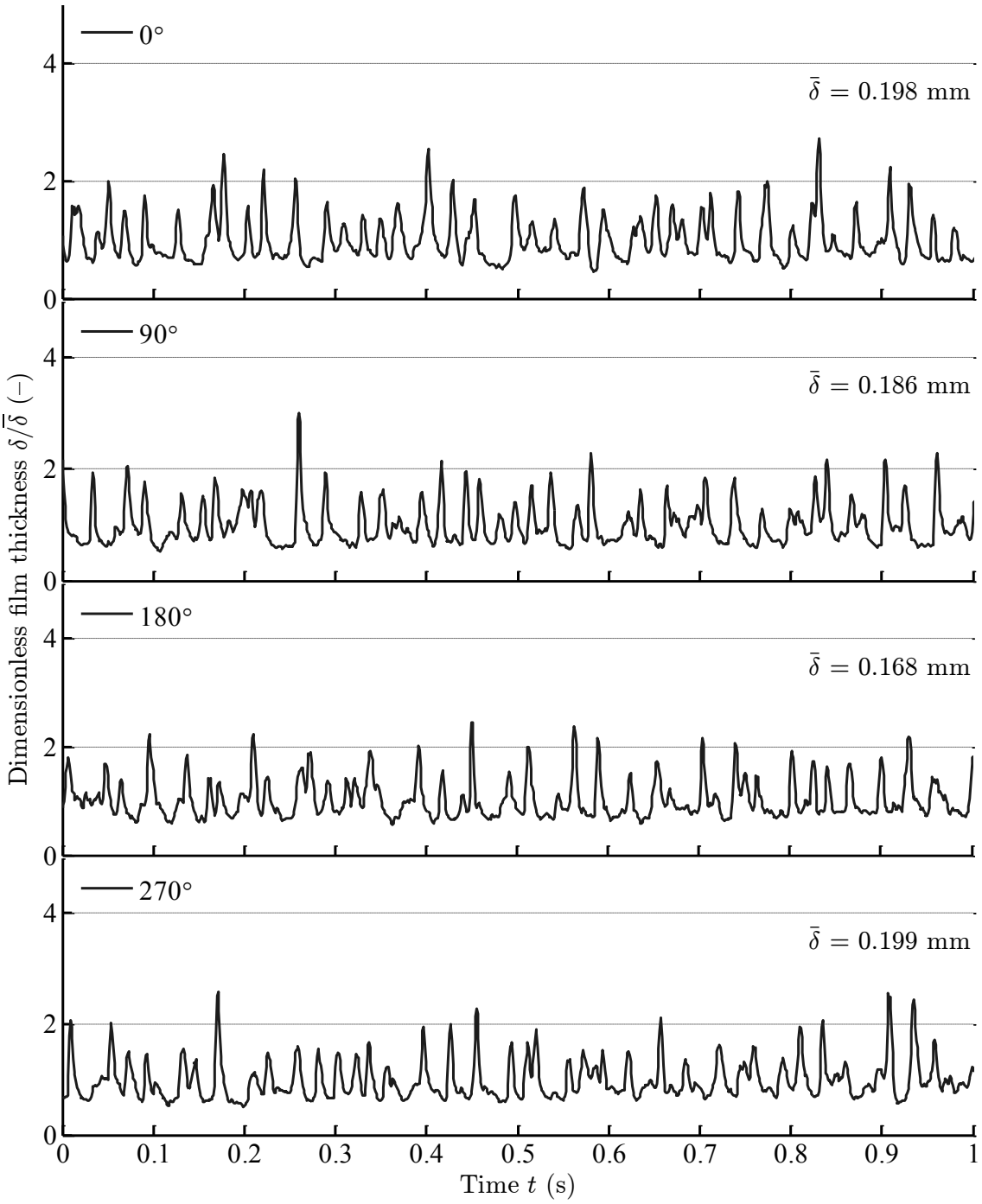
0°
$\bar{\delta}$ = 0.198 mm
90°
$\bar{\delta}$ = 0.186 mm
180°
$\bar{\delta}$ = 0.168 mm
270°
$\bar{\delta}$ = 0.199 mm
Dimensionless film thickness $\delta/\bar{\delta}$ (–)
Time t (s)
0
2
4
0.1
0.2
0.3
0.4
0.5
0.6
0.7
0.8
0.9
1

Figure 11

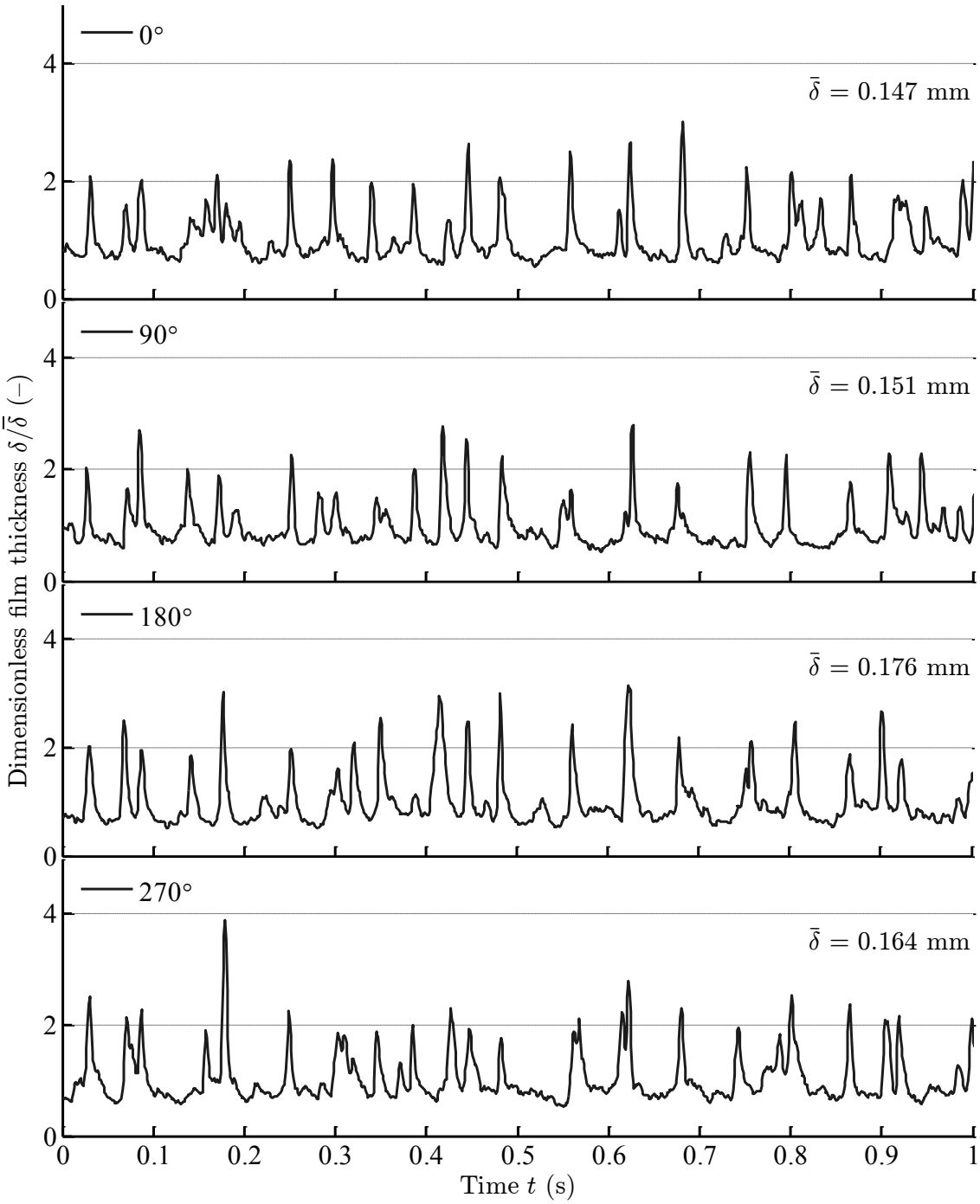
0°
$\bar{\delta} = 0.147$ mm
90°
$\bar{\delta} = 0.151$ mm
180°
$\bar{\delta} = 0.176$ mm
270°
$\bar{\delta} = 0.164$ mm
Dimensionless film thickness $\delta/\bar{\delta}$ (–)
Time t (s)
0
2
4
0.1
0.2
0.3
0.4
0.5
0.6
0.7
0.8
0.9
1

Figure 12

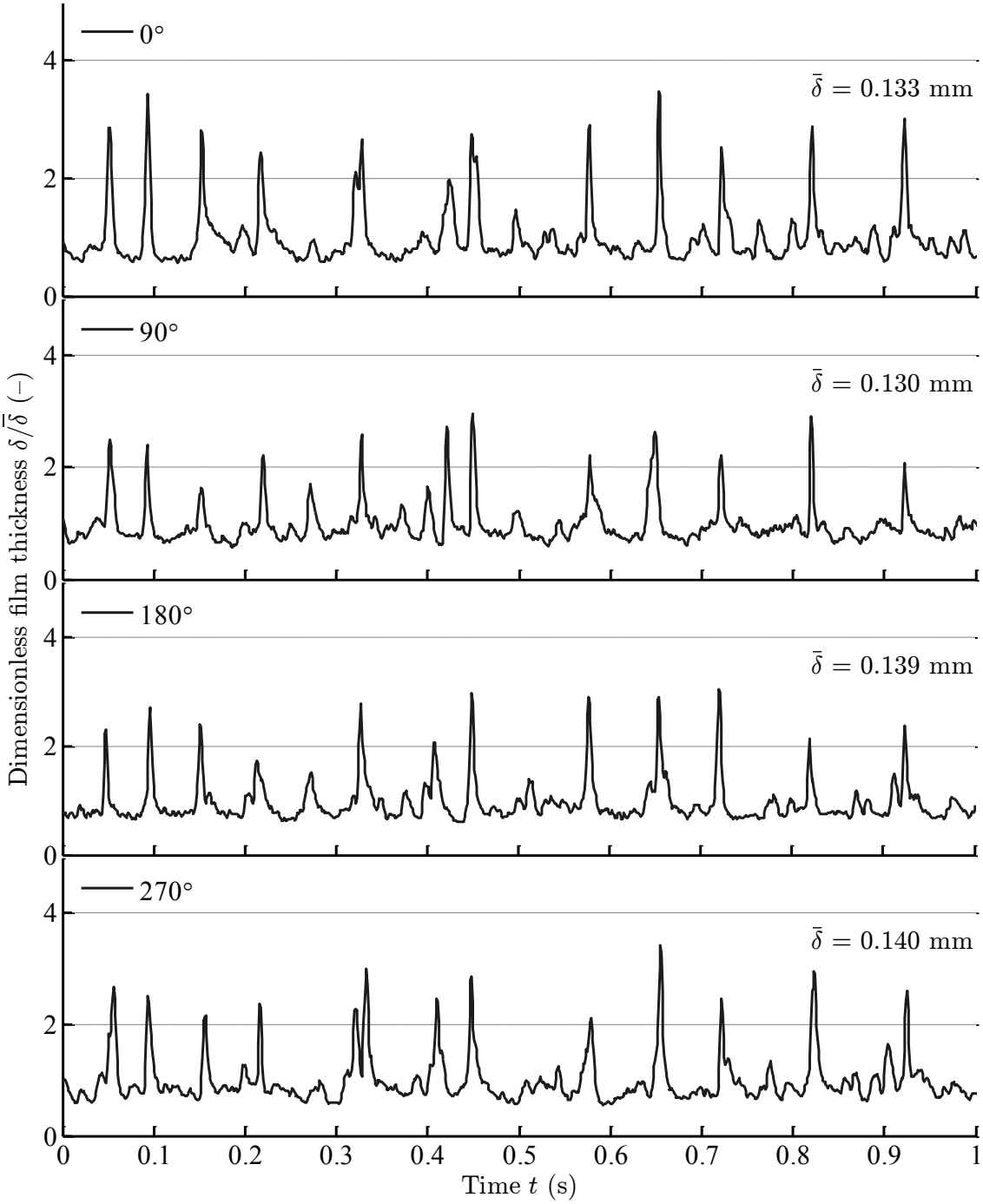
0°
$\bar{\delta} = 0.133$ mm
90°
$\bar{\delta} = 0.130$ mm
180°
$\bar{\delta} = 0.139$ mm
270°
$\bar{\delta} = 0.140$ mm
Dimensionless film thickness $\delta/\bar{\delta}$ (–)
Time t (s)
0
2
4
0.1
0.2
0.3
0.4
0.5
0.6
0.7
0.8
0.9
1

Figure 13

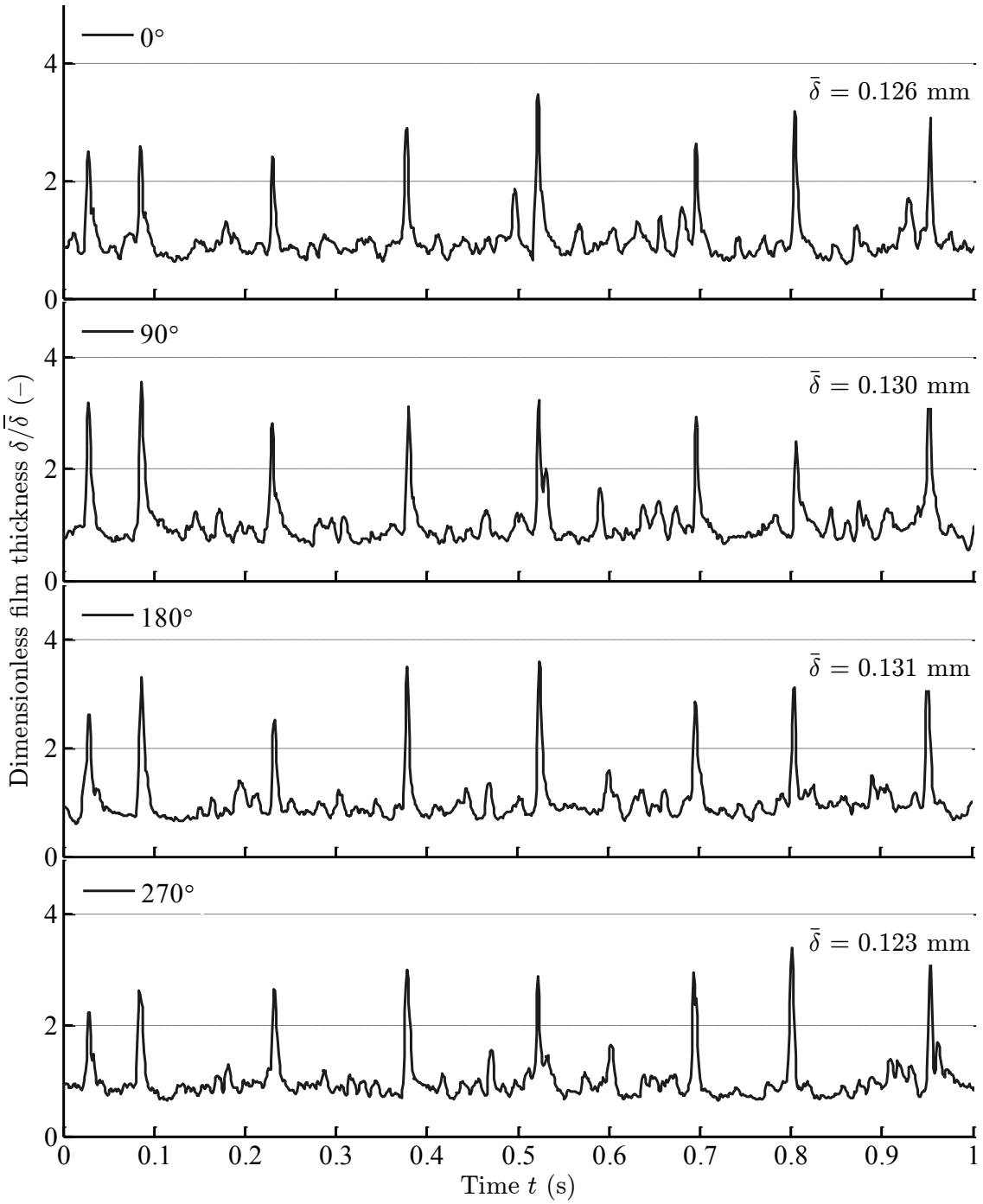
0°
$\bar{\delta} = 0.126$ mm
90°
$\bar{\delta} = 0.130$ mm
180°
$\bar{\delta} = 0.131$ mm
270°
$\bar{\delta} = 0.123$ mm
Dimensionless film thickness $\delta/\bar{\delta}$ (–)
Time t (s)
0
2
4
0.1
0.2
0.3
0.4
0.5
0.6
0.7
0.8
0.9
1

Figure 14

Figure 15

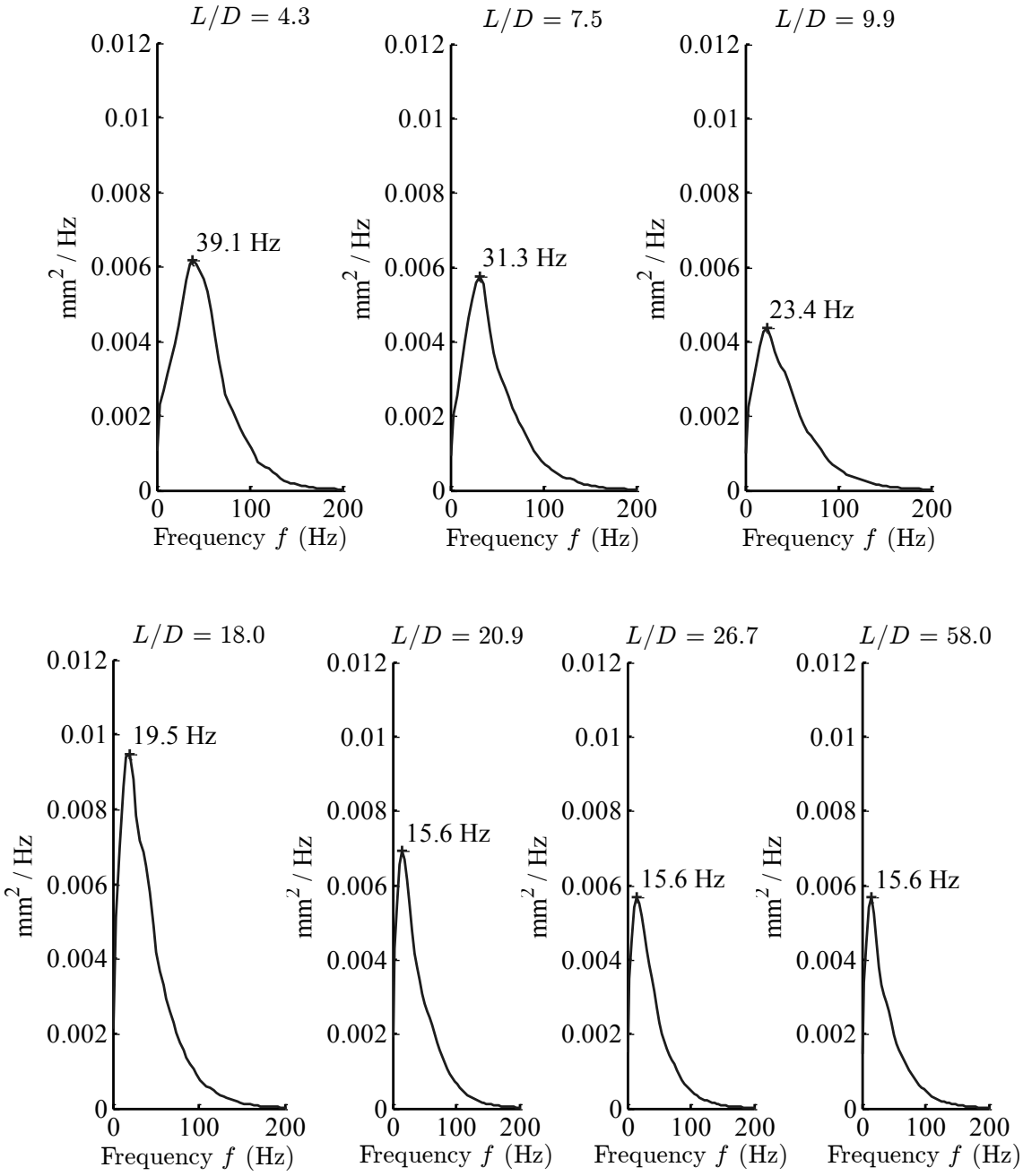

Figure 15

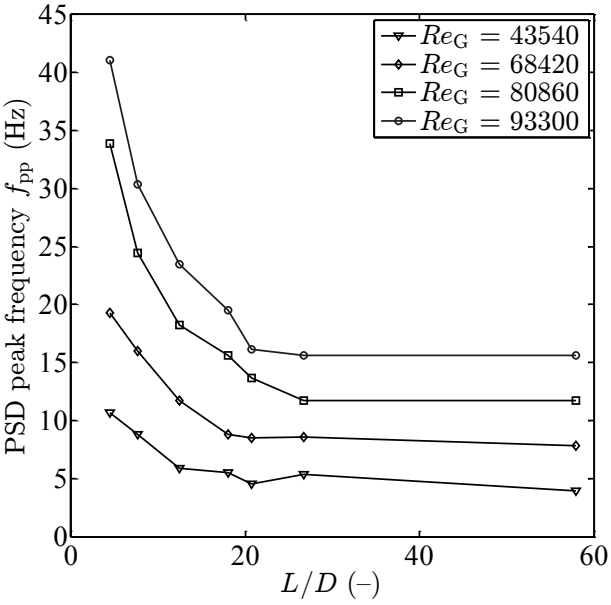
$Re_{\mathrm{G}} = 43540$
$Re_{\mathrm{G}} = 68420$
$Re_{\mathrm{G}} = 80860$
$Re_{\mathrm{G}} = 93300$
PSD peak frequency f_{pp} (Hz)
L/D (–)
0
5
10
15
20
25
30
35
40
45
0
20
40
60

Figure 16

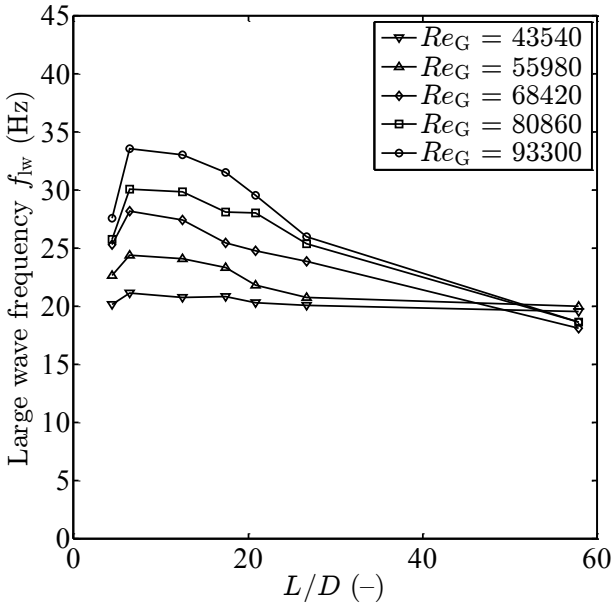
45
40
35
30
25
20
15
10
5
0
0
20
40
60
Large wave frequency f_{lw} (Hz)
L/D (–)
$Re_{\mathrm{G}} = 43540$
$Re_{\mathrm{G}} = 55980$
$Re_{\mathrm{G}} = 68420$
$Re_{\mathrm{G}} = 80860$
$Re_{\mathrm{G}} = 93300$

Figure 17

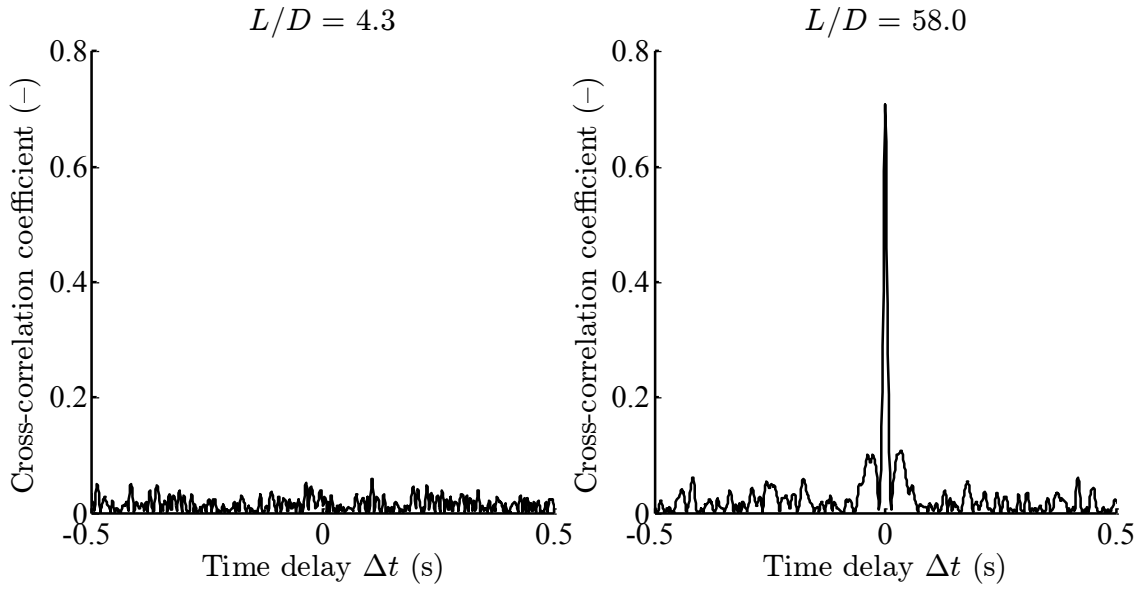
$L/D = 4.3$
$L/D = 58.0$
Cross-correlation coefficient (–)
Time delay Δt (s)
0.8
0.6
0.4
0.2
0
-0.5
0
0.5

Figure 18

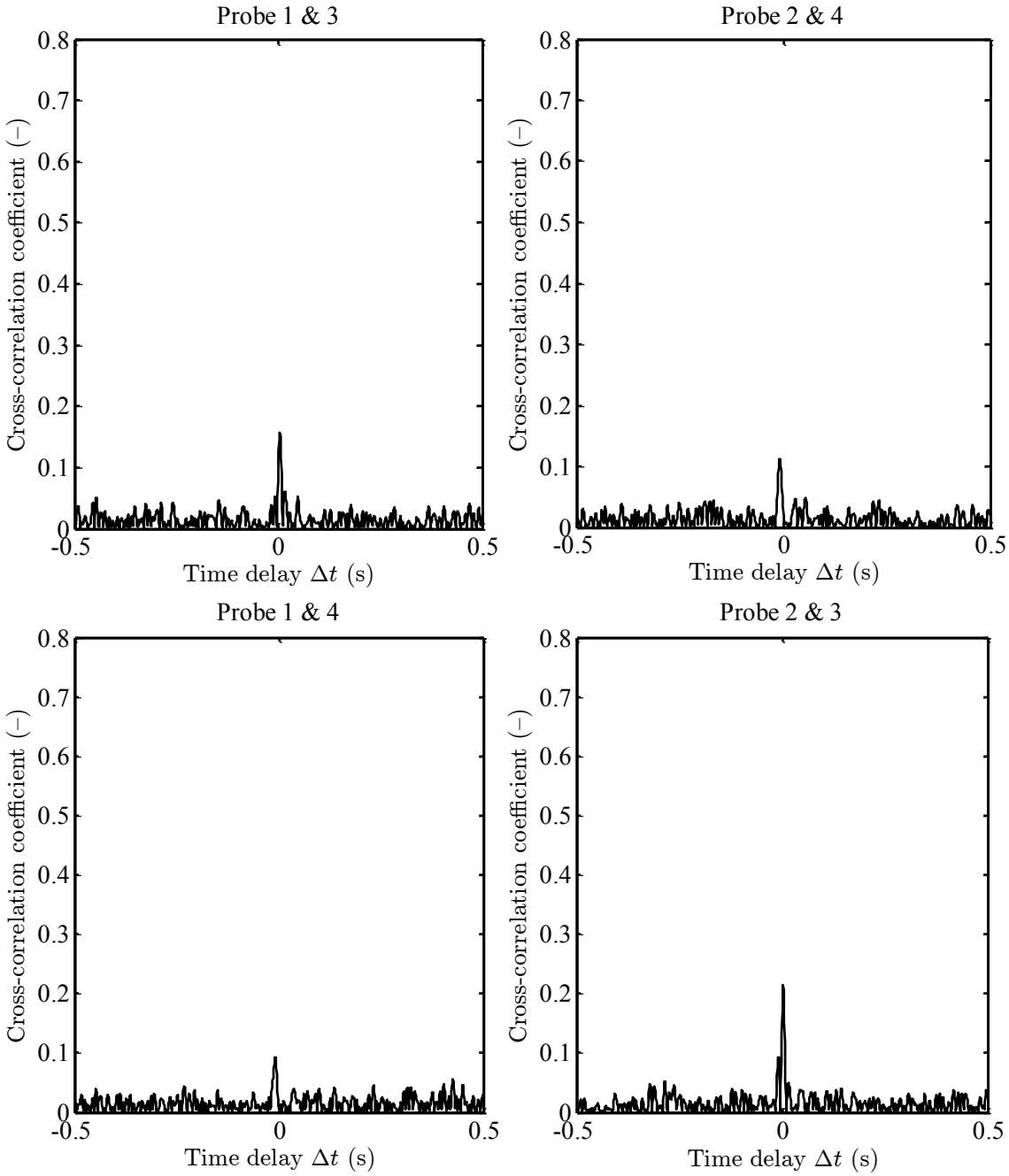
Probe 1 & 3
Probe 2 & 4
Probe 1 & 4
Probe 2 & 3
Cross-correlation coefficient (–)
Time delay Δt (s)
0.8
0.7
0.6
0.5
0.4
0.3
0.2
0.1
0
-0.5
0
0.5

Figure 19

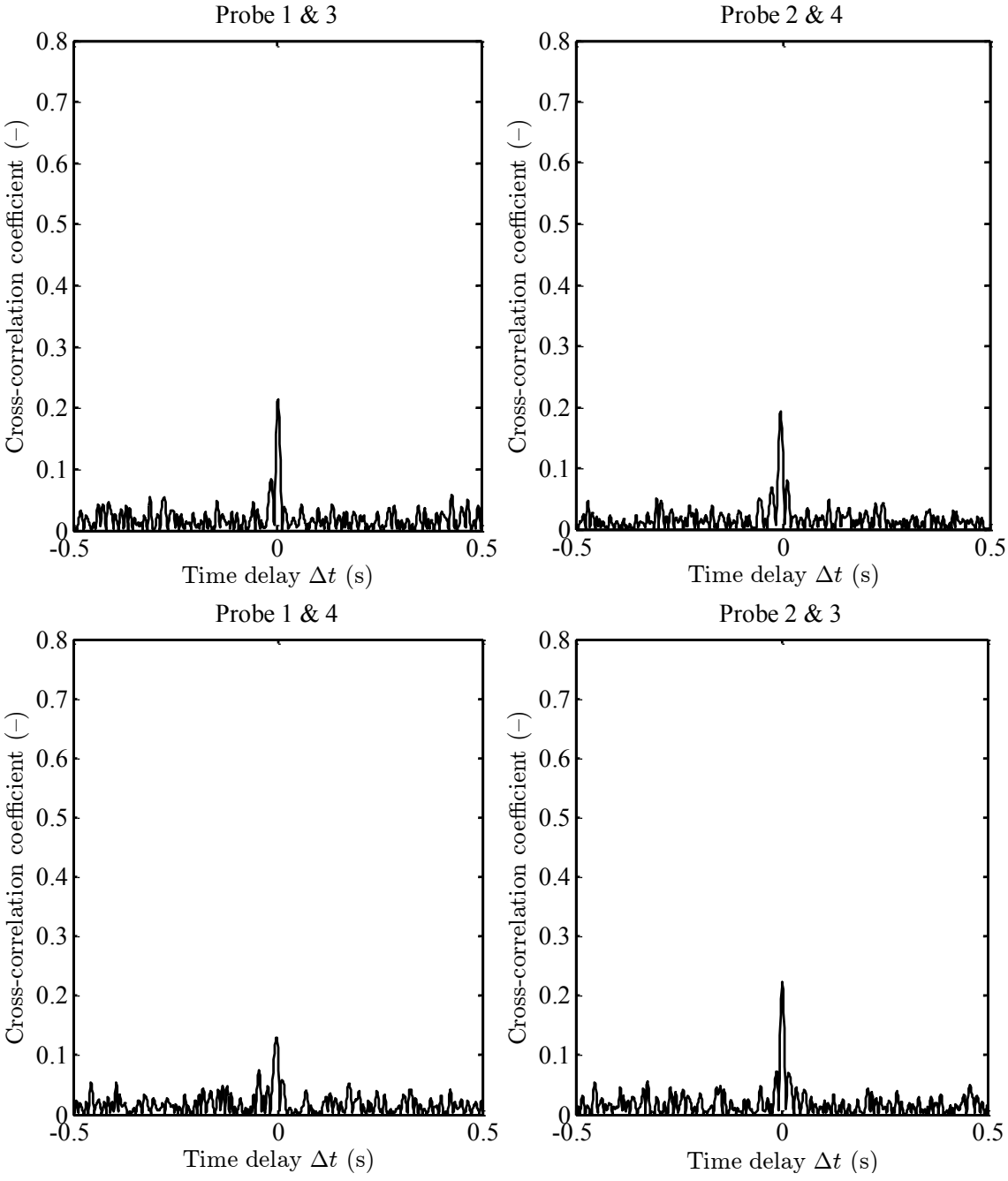
Probe 1 & 3
Probe 2 & 4
Probe 1 & 4
Probe 2 & 3
Cross-correlation coefficient (–)
Time delay Δt (s)
0.8
0.7
0.6
0.5
0.4
0.3
0.2
0.1
0
-0.5
0
0.5

Figure 20

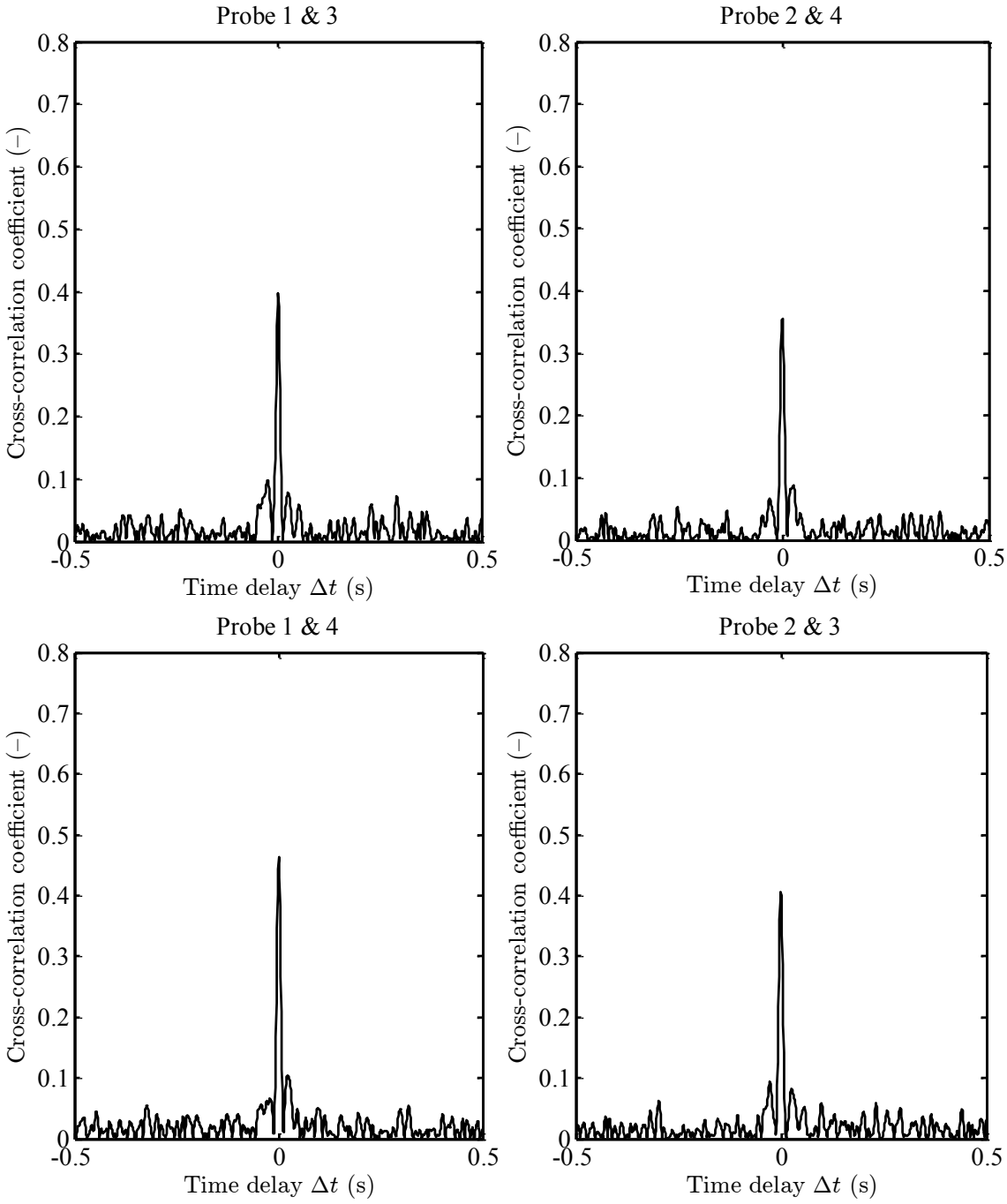
Probe 1 & 3
Probe 2 & 4
Probe 1 & 4
Probe 2 & 3
Cross-correlation coefficient (–)
Time delay Δt (s)
0.8
0.7
0.6
0.5
0.4
0.3
0.2
0.1
0
-0.5
0
0.5

Figure 21

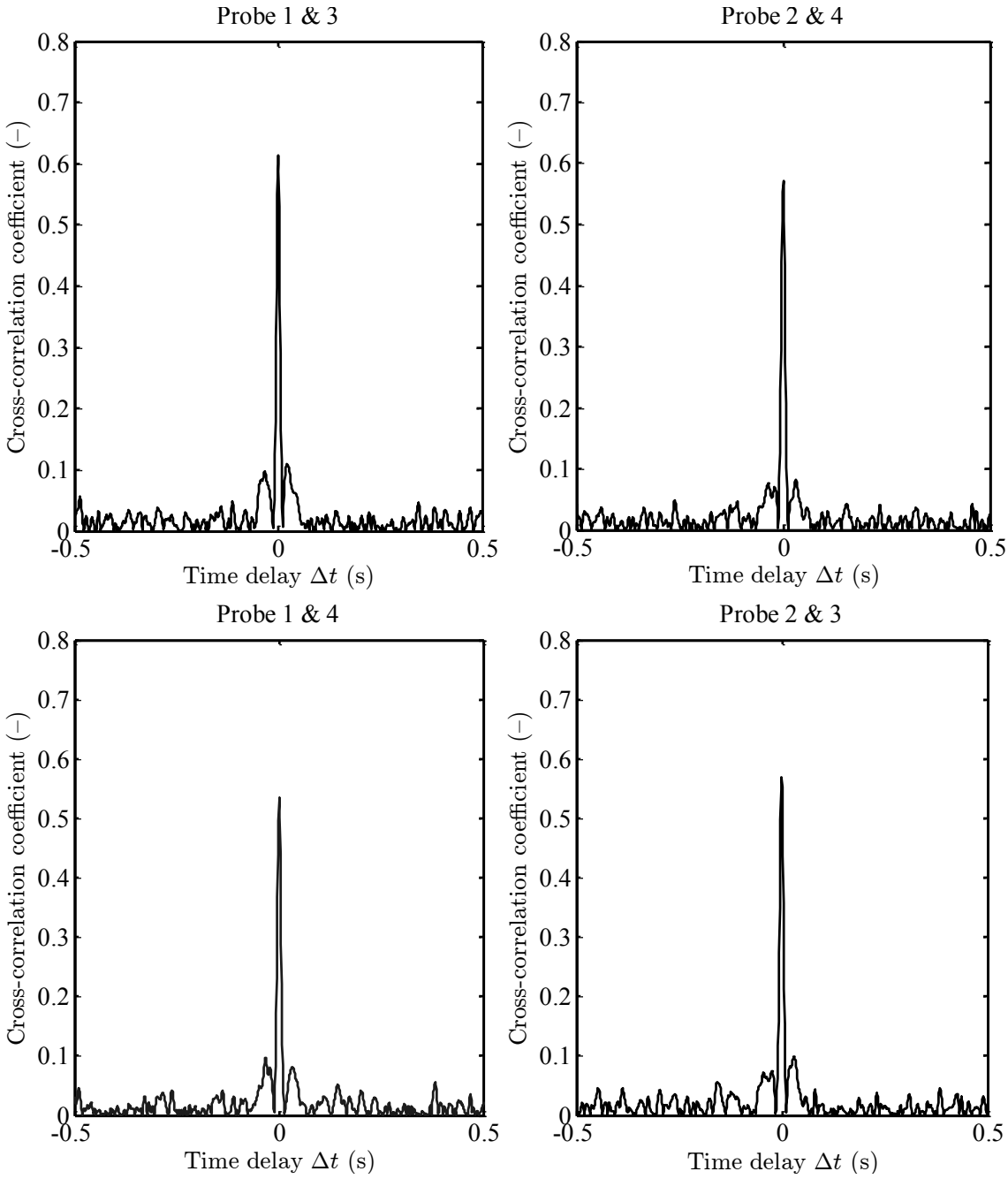
Probe 1 & 3
Probe 2 & 4
Probe 1 & 4
Probe 2 & 3
Cross-correlation coefficient (–)
Time delay Δt (s)
0.8
0.7
0.6
0.5
0.4
0.3
0.2
0.1
0
-0.5
0
0.5

Figure 22

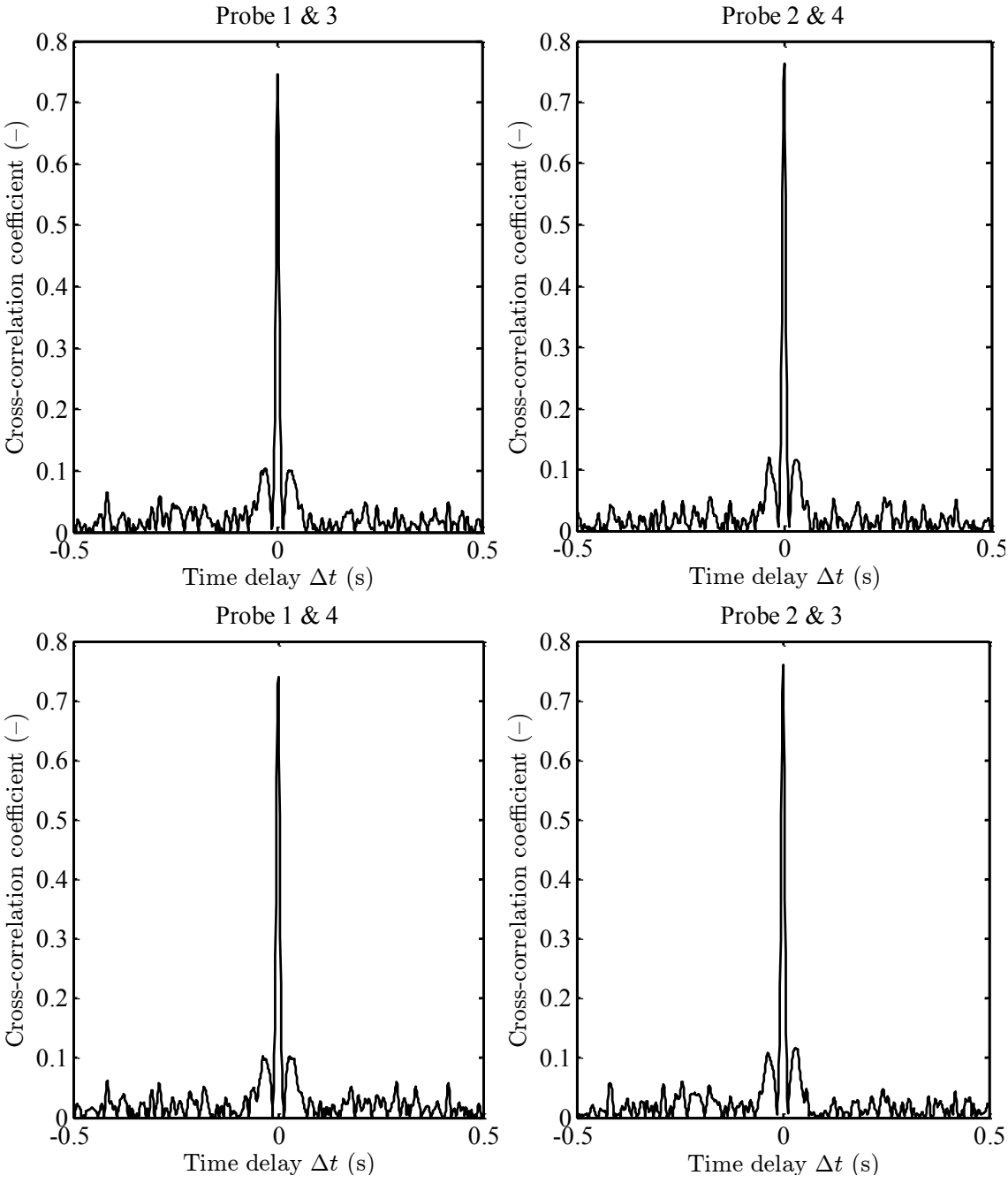
Probe 1 & 3
Probe 2 & 4
Probe 1 & 4
Probe 2 & 3
Cross-correlation coefficient (–)
Time delay Δt (s)
0.8
0.7
0.6
0.5
0.4
0.3
0.2
0.1
0
-0.5
0
0.5

Figure 23

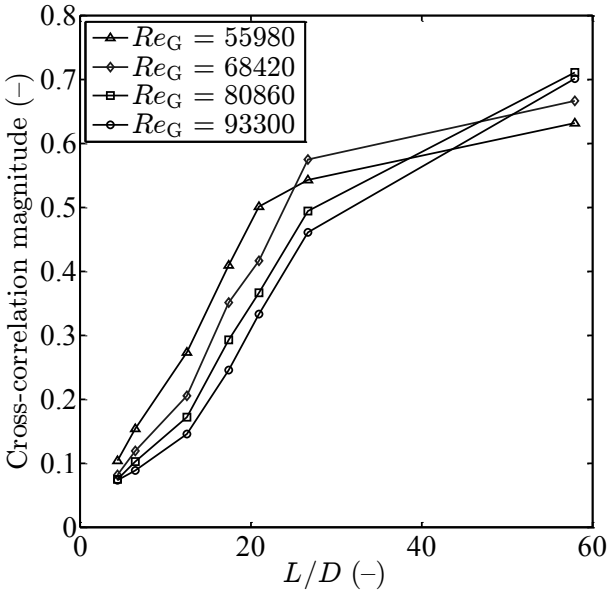
$Re_G = 55980$
$Re_G = 68420$
$Re_G = 80860$
$Re_G = 93300$
Cross-correlation magnitude (–)
L/D (–)
0
0.1
0.2
0.3
0.4
0.5
0.6
0.7
0.8
0
20
40
60

Figure 24

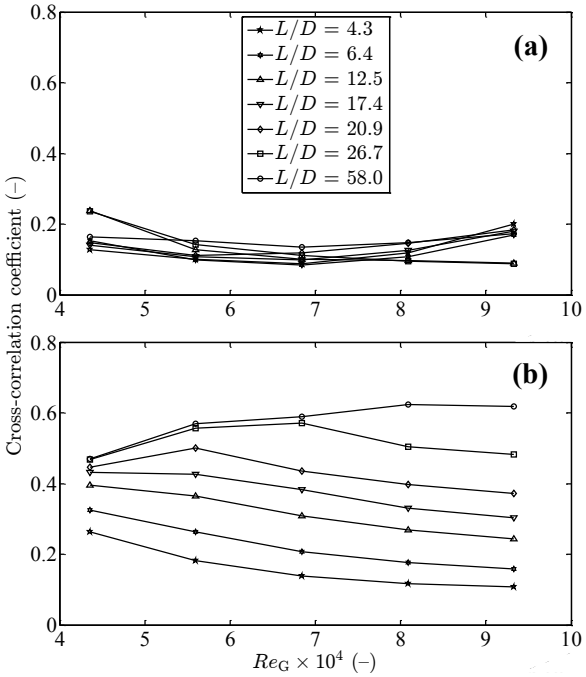
(a)
(b)
$L/D = 4.3$
$L/D = 6.4$
$L/D = 12.5$
$L/D = 17.4$
$L/D = 20.9$
$L/D = 26.7$
$L/D = 58.0$
Cross-correlation coefficient (–)
$Re_G \times 10^4$ (–)
0
0.2
0.4
0.6
0.8
4
5
6
7
8
9
10

Figure 25